Two-dimensional heat and mass transfer and thermodynamic analyses of porous microreactors with Soret and thermal radiation effects-An analytical approach

Graeme Hunt [a], Mohsen Torabi [1,b,c], Lilian Govone [a], Nader Karimi [1,a,d], Amirfarhang Mehdizadeh [d]

[a] School of Engineering, University of Glasgow, Glasgow G12 8QQ, United Kingdom

[b] The George W. Woodruff School of Mechanical Engineering, Georgia Institute of Technology, Atlanta, GA 30332, USA

[c] School of Engineering, University of California, Merced, CA 95343, USA

[d] School of Computing and Engineering, Civil and Mechanical Engineering Department, University of Missouri-Kansas City, Kansas City, MO 64110, USA

Abstract

Transport of heat and mass and the thermodynamics of porous microreactors with thermal diffusion and radiation effects are investigated analytically. The examined configuration includes an axisymmetric, thick-wall microchannel with an iso-flux thermal boundary condition imposed on the external surfaces. The microchannel is filled with porous materials and accommodates a zeroth order homogenous chemical reaction. Internal radiative heat transfer is modelled in addition to heat convection and conduction, while the local thermal non-equilibrium approach is taken within the porous section of the system. The transport of species is coupled with that of heat via the inclusion of thermodiffusion or Soret effect. Two-dimensional heat and mass transfer differential equations are solved analytically. The results are subsequently used to predict the thermodynamic irreversibilities inside the reactor and a thorough analysis of local and total entropy generation rates is performed. Also, the changes in Nusselt number, calculated on the internal walls of the microreactor, versus various parameters are reported. It is shown that the radiation effects can impact the temperature of the solid phase of the porous medium and lead to alteration of Nusselt number. It is further observed that the transfer of mass is the main source of irreversibility in the system. The findings are of particular use for the design and analysis of the microreactors with homogenous chemical reactions and can be also used for the validation of computational models.

Keywords: Microreactors; Coupled heat and mass transfer; Advection-diffusion-reaction model; Radiative heat transfer; Exact solution; Entropy generation.

Nomenclature

[1] Corresponding authors.
E-mails: Mohsen.Torabi@my.cityu.edu.hk, Mohsen.Torabi@gatech.edu (M. Torabi), Nader.Karimi@glasgow.ac.uk (N.Karimi).

a_{sf}	Interfacial area per unit volume of porous media, m^{-1}	Q	Wall heat flux ratio
Bi	Biot number	q_1''	Wall heat flux ($W\ m^{-2}$)
Br'	Modified Brinkman number	Re	Reynolds number
C	Mass species concentration ($kg\ m^{-3}$)	R	Specific gas constant ($J\ K^{-1}\ kg^{-1}$)
C_0	Inlet concentration ($kg\ m^{-3}$)	S	Shape factor of the porous medium
$C_{p,nf}$	Specific heat capacity ($J\ K^{-1}\ kg^{-1}$)	$\dot{S}_{Di}'''$	Volumetric entropy generation due to mass diffusion ($W\ K^{-1}\ m^{-3}$)
D	Effective mass diffusion coefficient ($m^2\ s^{-1}$)	$\dot{S}_{FF}'''$	Volumetric entropy generation due to fluid friction ($W\ K^{-1}\ m^{-3}$)
Da	Darcy number	$\dot{S}_{nf}'''$	Volumetric entropy generation in the nanofluid ($W\ K^{-1}\ m^{-3}$)
D_T	Coefficient of thermal mass diffusion ($kg\ K^{-1}\ m^{-1}\ s^{-1}$)	$\dot{S}_s'''$	Volumetric entropy generation in the porous solid ($W\ K^{-1}\ m^{-3}$)
h_1	Half-thickness of the microchannel (m)	$\dot{S}_w'''$	Volumetric entropy generation rate of the wall ($W\ K^{-1}\ m^{-3}$)
h_2	Half-height of the microchannel (m)	Sr	Soret number
h_{sf}	Interstitial heat transfer coefficient ($W\ K^{-1}\ m^{-2}$)	T	Temperature (K)
H_w	Wall heat transfer coefficient ($W\ K^{-1}\ m^{-2}$)	u	Nanofluid velocity ($m\ s^{-1}$)
k	Effective thermal conductivity ratio of the nanofluid and the porous solid	$\bar{u}$	Average velocity over cross-section ($m\ s^{-1}$)
k_1	Thermal conductivity of wall ($W\ K^{-1}\ m^{-1}$)	X	Dimensionless axial coordinate
k_{e1}	Ratio of thermal conductivity of wall 1 and thermal conductivity of the porous solid	x	Axial coordinate
k_{enf}	Effective thermal conductivity of the nanofluid phase ($W\ K^{-1}\ m^{-1}$)	Y	Dimensionless transverse coordinate
k_{es}	Effective thermal conductivity of the solid phase of the porous medium ($W\ K^{-1}\ m^{-1}$)	y	Transverse coordinate
k_r	Reaction rate constant ($kg\ m^{-3}\ s^{-1}$)		***Greek symbols***
L	Length of the microchannel (m)	μ	Dynamic viscosity ($N\ s\ m^{-2}$)
M	Viscosity Ratio	κ	Permeability (m^2)
N_{DI}	Dimensionless diffusive irreversibility	ρ	Density ($kg\ m^{-3}$)
N_{FF}	Dimensionless fluid friction irreversibility	θ	Dimensionless temperature
N_{int}	Dimensionless interstitial (interphase) heat transfer irreversibility	Φ	Dimensionless concentration
N_{nf}	Dimensionless nanofluid and interstitial (interphase) irreversibility	ξ	Aspect ratio of the microchannel
$N_{nf,ht}$	Dimensionless nanofluid heat transfer irreversibility	ε	Porosity of the porous medium
N_s	Dimensionless porous solid and interstitial (interphase) irreversibility	γ	Damköhler number
$N_{s,ht}$	Dimensionless heat transfer irreversibility	ω	Dimensionless heat flux
N_w	Dimensionless wall irreversibility	φ	Irreversibility distribution ratio
N_{pm}	Dimensionless total porous medium irreversibility		***Subscripts***
N_{Tot}	Dimensionless total entropy	s	Porous solid
Nu	Nusselt number	nf	Nanofluid
p	Pressure (Pa)	1	Wall
Pe	Peclet number	w	Wall
Pr	Prandtl number		

1. Introduction

With the provision of less costly and commercial micro manufacturing techniques, micro process engineering facilities are becoming more popular in both academia and industry [1]. Amongst these,

microreactors are one of the recently growing tools [2][3]. They have a broad range of applications from distributed fuel production [4] and methanol steam reforming [5] to process intensification [3] and nanoparticle generation [6]. In comparison with traditional reactors, microreactors occupy smaller volumes and feature other advantages such as performance enhancement, better temperature control and operation under continuous flow mode [7][8]. Hence, there exist major incentives for the development of micro-structured chemical reactors [9][10]. However, due to their smaller size, micro-structured reactors are rather sensitive to the changes in the surrounding temperature and thermal modifications of their external boundaries can affect their performance [3][4]. This is due to the fact that their heat and mass transfer characteristics are strongly coupled with their thermal boundary conditions as well as the details of internal transport mechanisms. These points have been emphasised in the recent studies on the effects of boundary conditions upon the energetic and entropic performances of microreactors [11][12] and also the influences of Soret effect on the concentration of species in microreactors [13].

Microreactors normally consist of a bundle of microchannels [14]. By filling these microchannels with porous materials, the microreactor provides a more uniform temperature distribution compared with the non-porous ones [15][16]. Further, the porous medium is often added as a means of introducing catalysts [17]. Recent examples can be found in continuous flow hydrogenation systems [18][19]. At the same time, porous microreactors can be an efficient tool for processes with large heat of reactions as they offer highly improved ability to transport heat by their massive surface to volume ratio [20]. It has been demonstrated that the internal heat transfer mechanisms could drastically impact the energetic and entropic performances of porous microchannels [21][22]. Hence, it is important to include all participant modes of heat transfer in the thermal analysis of these systems. The release of a large heat of reaction within the porous medium of the microreactor significantly increases the temperatures of both porous solid and fluid phases. This magnifies the role of thermal radiation [23] and warrants the inclusion of this mechanism of heat transport in thermal analysis of the microreactor.

To analyse a single porous reactor there are two well-known volume average approaches to follow [16]. The first traditional approach is to consider the porous solid and the fluid phases as a single phase material and specify average thermophysical properties to each point of the porous section of the reactor [13][24]. As this approach is not accurate enough in media with internal heat generations, a second method has been practiced recently. In this relatively new approach, the solid and fluid phases within the porous medium are analysed separately, and specific thermophysical properties are assigned to each phase [11][12]. The

transport of heat in solid and fluid phases of the porous medium are co-related through an internal heat exchange, and hence their differential equations are coupled. In general, the second approach, called the two-energy or local thermal non-equilibrium (LTNE) model, is more costly than the first one, i.e., local thermal equilibrium (LTE) model. However, due to its higher accuracy, LTNE approach is deemed more suitable in micro systems [25]. As in many microreactors the transfer of mass and heat are coupled [13], employing LTNE model can also provide a better prediction of the species concentration within the system.

So far, the analyses of porous microreactors and microchannels have been mainly concerned with temperature calculations [11][12]. A number of scholars have explored the effects of various phenomena including viscous dissipation [26], interface boundary conditions [27] and inclusion of nanoparticles [28][29] on the temperature fields and entropy generation rate inside porous micro systems. These studies have been recently extended to take into account the effects of solid walls of the microchannel on their first and second law performances [12][24][30]. However, so far, there has been only one investigation on the thermo-diffusion of microreactors [13]. In a one-dimensional analytical work, Torabi et al. [13] investigated the temperature field and entropy generation of double diffusive forced convection in a porous microchannels with the inclusion of Soret effect. In this work, the solid walls of the microchannel were considered in the mathematical model and two types of boundary conditions were imposed on the external surface of the microchannel. As an imperative shortcoming, currently, multi-dimensional double diffusive analyses of microreactors cannot be found in the open literature.

Zeroth order kinetic behaviour is prevalent in biological systems such as enzyme-catalysed reactions [31]. A catalytic surface may also cause reactions to exhibit zero order kinetics [31] due to limited availability of active sites. This is not, however, only a feature of large catalytic surfaces (such as channel wall catalysts) but is also the case when the catalyst is a small particle (as is the case in a slurry) [32]. With such systems in mind, the kinetics chosen for this study are zeroth order.

The preceding survey of literature reveals that there is now significant evidence showing that the solid body of micro-structured reactors should be included in the thermal analyses of these systems. Further, accurate performance prediction of microreactors with highly exothermic reactions is subject to conduction of comprehensive thermal analyses which take into account thermal radiation. However, theoretical examinations of radiative effects in porous microreactors are scarce. Finally, the existing studies on coupled heat and mass transfer and entropy generation in microreactors are all one-dimensional and multi-dimensional theoretical studies are yet to be conducted. To fill these gaps, the present work puts forward a

two-dimensional investigation on the influences of thermal radiation upon heat and mass transfer, and entropic behaviour of porous microreactors with thick walls.

The rest of this paper is organised as follows. Section 2 provides the details of the configuration under investigation together with the assumptions and governing equations. In Section **Error! Reference source not found.** the governing equations are non-dimensionalised. This is followed by Section 3, which gives the analytical solution methodology. Temperature and concentration fields, as well as the Nusselt number and entropy generations are discussed in Section 4, while Section 5 summarises the main findings.

2. Theoretical methods

2.1. Problem configuration and assumptions

Figure 1 shows the porous microreactor under investigation with thick walls and symmetric isoflux thermal boundary condition. It is assumed that the process in the microreactor can include high temperature reactions. Thus, the internal radiation plays an important role in the overall heat transfer process. For the purposes of the following analysis, Rosseland approximation has been used to model the thermal radiation. As LTNE model is adopted in this investigation, internal convective heat exchanges between the fluid and solid phases of the porous medium have been also considered in the mathematical model. The thicknesses of the solid walls of the reactor are incorporated in the model and the mass diffusion has been coupled with temperature field of the fluid through assuming a finite Soret number [13]. The other assumptions include steady, laminar, fully developed and incompressible fluid flow. Homogeneity of the properties of the materials, existence of no sharp reaction zones, absence of gravitational effects [11] [12], and reversibility of the homogenous chemical reaction are also assumed. In the current setting the heat of reaction may appear as a constant source term in the energy equation of the fluid phase. Nonetheless, this has been extensively studied in a number of previous investigations [11][12] [22][30][33] and hence it is not further considered in the current work. Thus for the purposes of this study heat of reaction has not been included. Further, in the followings the fluid phase is assumed to be a nanofluid. This is not an essential element of the analysis and can be readily removed by setting the volume fraction of nanoparticles to zero. Nonetheless, it has been added to the analysis to make it applicable to the microreactors that involve nanoparticles [6][34].

2.2. Governing Equations

Definition of the parameters introduced in this and the proceeding sections can be found in the nomenclature. The Darcy-Brinkman model of transport of momentum describes the hydrodynamics of the flow in microreactor. That is

$$-\frac{\partial p}{\partial x}+\mu_{eff}\frac{d^2u}{dy^2}-\frac{\mu_{nf}}{\kappa}u=0 \qquad 0\le y<h_1 \qquad (1)$$

The differential energy equations for the solid walls of the microreactor and the solid and fluid phases of the porous section of the system are expressed by the followings [11,35].

$$k_1\frac{\partial}{\partial y}\left[\frac{\partial T_1}{\partial y}\right]=0, \qquad h_1<y\le h_2 \qquad (2a)$$

$$k_{enf}\frac{\partial^2 T_{nf}}{\partial y^2}+h_{sf}a_{sf}\left(T_s-T_{nf}\right)+\frac{\mu_{nf}}{\kappa}u^2+\mu_{eff}\left(\frac{du}{dy}\right)^2=\rho_{nf}C_{p,nf}u\frac{\partial T_{nf}}{\partial x}, \qquad 0\le y<h_1 \qquad (2b)$$

$$k_{es}\frac{\partial^2 T_s}{\partial y^2}-h_{sf}a_{sf}\left(T_s-T_{nf}\right)-\frac{\partial q}{\partial y}=0. \qquad 0\le y<h_1 \qquad (2c)$$

Appendix A shows how the nanofluid thermophysical properties are calculated based on those of the base fluid and nanoparticles. It should be clarified that the third and fourth terms in the energy equation of the nanofluid phase account for the heat generation by viscous dissipation [35].

The radiation parameter in Eq. (2c) takes the form of

$$q_r=\frac{-4\,\sigma^*}{3\,\kappa^*}\frac{\partial T_s^4}{\partial y}. \qquad (3)$$

Using Rosseland approximation [36] the last term of the energy equation for the solid phase of the porous section of the microchannel is transformed to:

$$\frac{\partial q_r}{\partial y}=-\frac{16\sigma^* T_0^3}{3\,\kappa^*}\frac{\partial^2 T_s}{\partial y^2}. \qquad (4)$$

The radiative heat flux from the solid phase of the porous medium is caused by the solid phase having the ability to lose (or absorb) heat through radiation. In the current model, the fluid is assumed to be transparent to radiation, which is readily justifiable by considering the fact that most fluids are optically highly transparent [36]. Of course, that is not to say that the fluid phase is unaffected by the radiative heat loss form the solid phase, merely that the effect is indirect. Examination of the equations (2b) and (2c) reveal the terms for interstitial heat transfer between the phases, i.e., $h_{sf}a_{sf}(T_s\text{-}T_{nf})$. We have also considered the radiation heat transfer on the walls by including the radiation effect on the boundary condition Eq. (6b).

The production and transport of chemical species in the reactor is governed by the following advection-diffusion-reaction model for a zeroth order, homogenous, temperature indifferent chemical reaction. The

model takes into account the contributions from the Soret effect in addition to the Fickian diffusion of species [37].

$$u\frac{\partial C}{\partial x} = D\frac{\partial^2 C}{\partial y^2} - D_T\frac{\partial^2 T_{nf}}{\partial y^2} + k_r \qquad 0 \le y < h_1 \qquad (5)$$

It is recalled that depending on the relative size of the diffusive molecules and those of the base fluid, Soret number can be either positive or negative [37]. In Eq. (5) negative thermodiffusion coefficient is presented by a negative sign in front of a positive D_T.

The following boundary conditions are necessary for the closure of the momentum and energy equations of the system [11,35]:

$$y = h_2: \quad k_1\frac{\partial T_1}{\partial y}\Big|_{y=h_2} = q_1'' \qquad (6a)$$

$$y = h_1: \quad u_{nf} = 0, \quad T_{nf} = T_s = T_w, \quad q_1'' = k_{enf}\frac{\partial T_{nf}}{\partial y}\Big|_{y=h_1} + (k_{es} + \frac{16\sigma^*}{3\,\kappa^*})\frac{\partial T_s}{\partial y}\Big|_{y=h_1} \qquad (6b)$$

$$y = 0: \quad \frac{du_{nf}}{dy} = 0, \quad \frac{\partial T_{nf}}{\partial y}\Big|_{y=0} = \frac{\partial T_s}{\partial y}\Big|_{y=0} = 0, \qquad (6c)$$

For a zeroth order chemical reaction, the imposed conditions for the concentration of chemical species are the followings.

$$x = 0, y = h_1 \qquad C = C_0 \qquad (7a)$$

$$y = 0 \qquad \frac{\partial C}{\partial y} = 0 \qquad (7b)$$

It is recalled that in the current problem the terms in energy transport equation are generally much larger than those in mass transport equation. As a result, the relatively small contribution of Dufour effect with the energy balance has been ignored. However, the influence of Soret effect upon mass transport equation remains noticeable and therefore it has been taken into account. This argument has been already made in a number of previous investigations, see for example [38][39][40][41].

3. Dimensionless parameters and non-dimensionalised equations

The following dimensionless parameters are introduced to enable universal analysis of the system under investigation.

$$\theta_i = \frac{(T_i - T_{w,in})k_{es}}{q_1'' h_2}, \quad u_r = -\frac{h_2^2}{\mu_f}\frac{\partial p_{nf}}{\partial x}, \quad Bi = \frac{h_{sf} a_{sf} {h_2}^2}{k_{es}}, \quad \gamma = \frac{k_r h_1^2}{D C_0},$$

$$Y = \frac{y}{h_2}, \quad Da = \frac{\kappa}{h_2^2}, \quad Br' = \frac{\mu_{eff}\bar{u}^2}{q_1'' h_2}, \quad Sr = \frac{q_1'' h_1 D_T}{C_0 k_{nf} D},$$

$$Y_1 = \frac{h_1}{h_2}, \quad M = \frac{\mu_{eff}}{\mu_{nf}}, \quad k_{e1} = \frac{k_1}{k_{es}}, \quad k = \frac{k_{enf}}{k_{es}} = \frac{\varepsilon k_{nf}}{(1-\varepsilon)k_s}, \tag{8}$$

$$X = \frac{x}{L}, \quad S = \frac{1}{\sqrt{MDa}}, \quad \Phi = \frac{C}{C_0}, \quad Re = \frac{2h_2 \rho_{nf} \bar{u}^2}{\mu_{eff}},$$

$$\xi = \frac{h_2}{L}, \quad Pr = \frac{C_{p,nf}\mu_{eff}}{k_{enf}} \quad Rd = \frac{16\,\sigma^*}{3\,\kappa^* k_{es}} \quad Pe = \frac{\bar{u} h_1}{D},$$

$$U = \frac{u}{u_r},$$

where the dimensionless temperature follows the labelling convention of *i= 1, s , n_f*.

The transport of momentum (Eq. (1)) is non-dimensionalised using the parameters defined in Eqs. (8), resulting in

$$M\frac{d^2U}{dY^2} - \frac{U}{Da} + 1 = 0. \qquad 0 \le Y < Y_1 \tag{9}$$

The no slip boundary condition at the solid-porous interfaces and the condition due to the axial symmetry at $Y = 0$ can be expressed in non-dimensional form as

$$U(Y_1) = 0, \tag{10a}$$

$$U'(0) = 0. \tag{10b}$$

Solution of Eq. (9) results in the following expression for the non-dimensional flow velocity

$$U = Da\left(1 - \frac{\cosh(SY)}{\cosh(SY_1)}\right). \qquad 0 \le Y < Y_1 \tag{11}$$

Using Eq. (11), the dimensionless average velocity across the channel reduces to

$$\bar{U} = Da\left(1 - \frac{\tanh(SY_1)}{SY_1}\right). \tag{12}$$

By combining Eqs. (11) and (12) the following ratios are formed

$$u/\bar{u} = U/\bar{U} = \frac{SY_1(\cosh(SY_1) - \cosh(SY))}{SY_1\cosh(SY_1) - \sinh(SY_1)}. \tag{13}$$

Due to the assumption of fully developed flow the following conditions hold [35],

$$\frac{\partial T_{nf}}{\partial x} = \frac{d\bar{T}_{nf}}{dx} = \frac{\partial T_s}{\partial x} = \frac{d\bar{T}_s}{dx} = \frac{dT_w}{dx} = \Omega = \text{constant}. \tag{14}$$

Equations (14) allows for the following form of the solution to be sought for the temperature field,

$$T_i(x,y) = f_i(y) + \Omega x \qquad i = 1, s, nf, \tag{15}$$

where $f_i(y)$ is a function to be determined by solving Eqs. (2a) to (2c) in association with the given boundary conditions. In order to solve the transports of thermal energy in the porous medium, first it is necessary to add Eqs. (2b) to (2c) and then integrate the resultant equation over the cross-section of the microchannel. Substituting in the heat flux boundary condition from Eq. (6a) yields

$$q_1'' + \frac{\mu_{nf}}{\kappa}\int_0^{h_1} u^2\, dy \; + \; \mu_{eff}\int_0^{h_1}\left(\frac{du}{dy}\right)^2 dy = \rho_{nf}C_{p,nf}\int_0^{h_1} u\frac{\partial T_{nf}}{\partial x}dy. \tag{16}$$

Rearranging Eq. (13) allows for the substitution for u into Eq. (16). Applying the non-dimensional parameters, as defined in Eqs. (8), facilitates the integration process and reveals:

$$\frac{d\bar{T}_{nf}}{dx} = \frac{1}{\rho_{nf}C_{p,nf}\bar{u}h_1h_2}\left[h_2q_1'' + \frac{\mu_{eff}S^3\bar{u}^2Y_1^2\cosh(SY_1)}{SY_1\cosh\,(SY_1) - \sinh(SY_1)}\right] = \Omega, \tag{17}$$

where the bulk mean temperature of the nanofluid is given by,

$$\bar{T}_{nf} = \frac{1}{\bar{u}h_1}\int_0^{h_1} uT_{nf}\, dy. \tag{18}$$

Combining Eqs. (9), (13) and (17) results in the non-dimensional form of Eqs. (2a-c):

$$k_{e1}\theta_1'' = 0 \qquad Y_1 < Y \le 1 \tag{19a}$$

$$k\theta_{nf}'' + Bi\left(\theta_s - \theta_{nf}\right) + D_2\cosh(2SY) + D_3\cosh(SY) + D_4 = 0 \qquad 0 \le Y < Y_1 \tag{19b}$$

$$(1+Rd)\theta_s'' - Bi\left(\theta_s - \theta_{nf}\right) = 0 \qquad 0 \le Y < Y_1 \tag{19c}$$

Through an algebraic manipulation of Eqs. (19b) and (19c), the following relations are developed.

$$k(1+Rd)\theta_{nf}'''' - Bi(1+k+Rd)\theta_{nf}'' + (4S^2(1+Rd) - Bi)D_2\cosh(2SY) \tag{20a}$$
$$+ (S^2(1+Rd) - Bi)D_3\cosh(SY) - BiD_4 = 0,$$

$$k(1+Rd)\theta_s'''' - Bi(1+k+Rd)\theta_s'' - Bi(D_2\cosh\,(2SY) + D_3\cosh\,(SY) + D_4) = 0. \tag{20b}$$

These provide decoupled solid and fluid energy equations in the porous medium. Particular solutions of Eqs. (19a) and (20a-b) require 10 boundary conditions as given by the followings.

$$\theta_{nf}(Y_1) = \theta_s(Y_1) = 0 \tag{21a,b}$$

$$\theta_s''(Y_1) = 0 \qquad \theta_{nf}''(Y_1) = -\frac{1}{k}(D_2\cosh(2SY) + D_3\cosh(SY) + D_4) \tag{21c,d}$$

$$\theta_1(Y_1) = 0 \qquad k_{e1}\theta_1'(1) = 1 \tag{21e,f}$$

$$\theta_{nf}'(0) = \theta_s'(0) = 0 \qquad \theta_{nf}'''(0) = \theta_s'''(0) = 0 \tag{21g,h}$$

Appendix B provides explicit expressions for the constant coefficients in Eqs. (21a-h).

3. Solution of momentum, energy and dispersion equations-calculation of entropy generation

Applying the boundary conditions given by Eqs. (21a-h) allows the analytical solutions of the system of Eqs. (19a) and (20a-b) to be found. The resulting closed-form dimensionless temperature profiles in the transverse direction are:

$$\theta_1(Y) = E_1 + E_2 Y \qquad Y_1 < Y \le 1 \qquad (22a)$$

$$\theta_{nf}(Y) = E_3 \cosh(2SY) + E_4 \cosh(SY) + E_5 \cosh(\alpha Y) + E_6 Y^2 + E_7 Y + E_8 \qquad 0 \le Y < Y_1 \qquad (22b)$$

$$\theta_s(Y) = E_9 \cosh(2SY) + E_{10} \cosh(SY) + E_{11} \cosh(\alpha Y) + E_6 Y^2 + E_7 Y + E_{12} \qquad 0 \le Y < Y_1 \qquad (22c)$$

in which

$$\alpha = \sqrt{\frac{Bi(1+k+Rd)}{k(1+Rd)}}. \qquad (23)$$

Through substitution of the dimensionless axial and transverse temperature profiles into Eq. (15), and incorporating Eq. (17) the two-dimensional temperature fields can be obtained. These are given by the following expressions.

$$\theta_1(X,Y) = \frac{2\,X\,[1 + Br' D_1\, S^2 \cosh(SY_1)]}{Re\,\mathrm{Pr}\,k\,Y_1 \xi} + E_1 + E_2 Y \qquad Y_1 < Y \le 1 \qquad (24a)$$

$$\theta_{nf}(X,Y) = \frac{2\,X\,[1 + Br' D_1\, S^2 \cosh(SY_1)]}{Re\,\mathrm{Pr}\,k\,Y_1 \xi} + E_3 \cosh(2SY) + E_4 \cosh(SY) + E_5 \cosh(\alpha Y) + E_6 Y^2 + E_7 Y + E_8 \qquad 0 \le Y < Y_1 \qquad (24b)$$

$$\theta_s(X,Y) = \frac{2\,X\,[1 + Br' D_1\, S^2 \cosh(SY_1)]}{Re\,\mathrm{Pr}\,k\,Y_1 \xi} + E_9 \cosh(2SY) + E_{10} \cosh(SY) + E_{11} \cosh(\alpha Y) + E_6 Y^2 + E_7 Y + E_{12} \qquad 0 \le Y < Y_1 \qquad (24c)$$

Similar to the previous section, the explicit form of the constant parameters are given in Appendix B. To calculate the Nusselt number on the microchannel wall, the heat transfer coefficient should firstly be evaluated. The heat transfer coefficient at the top wall of the microchannel is defined as

$$H_w = \frac{q_1''}{T_w - \bar{T}_{nf}} \qquad (25)$$

Thus, Nusselt number on the basis of the channel height h_1 is expressed by

$$Nu_w = \frac{2H_w h_1}{k_{enf}} = \frac{-2\,Y_1}{k\bar{\theta}_{nf}}. \qquad (26)$$

The dimensionless bulk mean temperature of the nanofluid, $\bar{\theta}_{nf}$ can be found by determining a dimensionless form of Eq. (18) and then integrating over the microchannel. This results in

$$\bar{\theta}_{nf} = \frac{D_1}{2\,Y_1}\int_0^{Y_1} \theta_{nf}[\cosh(SY_1) - \cosh(SY)]\,dY. \tag{27}$$

To evaluate the concentration profile first a control volume over a section of the microchannel should be considered. By doing so and applying a mass balance to this the following equation is obtained,

$$\bar{u}\frac{\partial C}{\partial x} = k_r. \tag{28}$$

The solution of Eq. (28) is

$$C(x) = \frac{k_r\,x}{\bar{u}}. \tag{29}$$

Thus, the concentration field in the axial direction is independent of the profile in the transverse direction and therefore the form of solution for the concentration field is similar to that of the temperature field:

$$C(x,y) = g(y) + h(x). \tag{30}$$

Using the dimensionless parameters defined in Eqs. (8), Eq. (29) can be non-dimensionalised in the following form.

$$\Phi(X) = \frac{\gamma\,X}{Pe\;Y_1\xi}. \tag{31}$$

Substitution of Eq. (29) into Eq. (5) gives

$$u\,\frac{k_r}{\bar{u}} = D\frac{\partial^2 C}{\partial y^2} - D_T\frac{\partial^2 T_{nf}}{\partial y^2} + k_r. \tag{32}$$

By employing the dimensionless parameters from Eqs. (8), Eq. (32) is first non-dimensionalised and then rearranged in the form of,

$$\Phi''(Y) - (\frac{u}{\bar{u}} - 1)\frac{\gamma}{Y_1^2} = \frac{Sr\,k}{Y_1\varepsilon}\theta_{nf}''(Y). \tag{33}$$

Since $\theta_{nf}''(Y)$ is determined from Eq. (24b) only the boundary conditions given by Eqs. (7a) and (7b) need non-dimensionalisation. These are expressed by,

$$\Phi'(0) = 0, \tag{34a}$$

$$\Phi(Y_1) = 1. \tag{34b}$$

Through applying Eqs. (34a) and (34b), Eq. (33) can be solved analytically to obtain the dimensionless concentration profile in the transverse direction. This reads

$$\Phi(Y) = F_1\cosh(2SY) + F_2\cosh(SY) + F_3\cosh(\alpha Y) + F_4Y^2 + F_5. \tag{35}$$

Finally, substituting Eqs. (31) and (35) into Eq. (30) gives the dimensionless, two-dimensional concentration field:

$$\Phi(X,Y) = \frac{\gamma\, X}{Pe\; Y_1 \xi} + F_1 \cosh(2SY) + F_2 \cosh(SY) + F_3 \cosh(\alpha Y) + F_4 Y^2 + F_5. \tag{36}$$

Appendix B provides analytical expressions for the constants appearing in the above equations. It should be noted that when resolving in the x direction Eq. (31) shows the analogous form to the x component of Eq. (24). In Eq. (24), $\theta(x) = 0$ at $x = 0$ and similarly for Eq. (31), $\Phi(x) = 0$ at $x = 0$ holds.

To calculate the local entropy generation rate the velocity, temperature and concentration equations should be incorporated into the fundamental entropy generation equations. The volumetric local entropy generation for the system are expressed by [11,13,35],

$$\dot{S}_w''' = \frac{k_1}{T_1^2}\left[\left(\frac{\partial T_1}{\partial x}\right)^2 + \left(\frac{\partial T_1}{\partial y}\right)^2\right], \tag{37a}$$

$$\dot{S}_S''' = \frac{k_{es}}{T_S^2}\left[\left(\frac{\partial T_S}{\partial x}\right)^2 + \left(\frac{\partial T_S}{\partial y}\right)^2\right] - \frac{h_{sf} a_{sf}\left(T_s - T_{nf}\right)}{T_S}, \tag{37b}$$

$$\dot{S}_{nf}''' = \frac{k_{enf}}{T_{nf}^2}\left[\left(\frac{\partial T_{nf}}{\partial x}\right)^2 + \left(\frac{\partial T_{nf}}{\partial y}\right)^2\right] + \frac{h_{sf} a_{sf}\left(T_s - T_{nf}\right)}{T_{nf}}, \tag{37c}$$

$$\dot{S}_{FF}''' = \frac{\mu_{nf}}{\kappa\, T_{nf}} u^2 + \frac{\mu_{eff}}{T_{nf}}\left(\frac{du}{dy}\right)^2, \tag{37d}$$

$$\dot{S}_{DI}''' = \frac{R\, D}{C}\left[\left(\frac{\partial C}{\partial x}\right)^2 + \left(\frac{\partial C}{\partial y}\right)^2\right] + \frac{R\, D}{T_{nf}}\left[\left(\frac{\partial C}{\partial x}\right)\left(\frac{\partial T_{nf}}{\partial x}\right) + \left(\frac{\partial C}{\partial y}\right)\left(\frac{\partial T_{nf}}{\partial y}\right)\right], \tag{37e}$$

In Eqs. (37), entropy generation terms have been split into contributions from different sources of irreversibility. The term $\dot{S}_w'''$ accounts for the entropy generation in the thick wall. Entropy generation in the solid phase of the porous medium due to heat transfer is accounted by $\dot{S}_s'''$, similarly $\dot{S}_{nf}'''$ represents the entropy generation rate in the nanofluid phase. The contribution made by irreversibility in the nanofluid due to fluid friction is expressed by $\dot{S}_{FF}'''$. The term $\dot{S}_{DI}'''$ is the entropy generation by the combination of concentration gradients and also that by mixed thermal and concentration gradients.

To non-dimensionalise Eqs. (37a-e) the following parameters are required. These are the dimensionless entropy generation, dimensionless heat flux and an irreversibility distribution ratio respectively.

$$N_i = \frac{\dot{S}_i''' h_2^2}{k_{es}}, \qquad i = w, s, nf, FF, DI \tag{38}$$

$$\omega = \frac{q_1'' h_2}{k_{es} T_{w,in}}, \tag{39}$$

$$\varphi = \frac{RDC_0}{k_{es}}. \tag{40}$$

The resultant non-dimensionalised forms of Eqs. (37a-e) are:

$$N_w = \frac{k_{e1}\omega^2}{(\omega\theta_1 + 1)^2}\left[\left(\frac{\partial\theta_1}{\partial X}\right)^2 + \left(\frac{\partial\theta_1}{\partial Y}\right)^2\right] \qquad Y_1 \le Y < 1 \qquad (41a)$$

$$N_s = \frac{\omega^2}{(\omega\theta_s + 1)^2}\left[\xi^2\left(\frac{\partial\theta_s}{\partial X}\right)^2 + \left(\frac{\partial\theta_s}{\partial Y}\right)^2\right] - \frac{Bi\ \omega\left(\theta_s - \theta_{nf}\right)}{(\omega\theta_s + 1)} \qquad 0 \le Y < Y_1 \qquad (41b)$$

$$N_{nf} = \frac{k\ \omega^2}{\left(\omega\theta_{nf} + 1\right)^2}\left[\xi^2\left(\frac{\partial\theta_{nf}}{\partial X}\right)^2 + \left(\frac{\partial\theta_{nf}}{\partial Y}\right)^2\right] + \frac{Bi\ \omega\left(\theta_s - \theta_{nf}\right)}{\left(\omega\theta_{nf} + 1\right)} \qquad 0 \le Y < Y_1 \qquad (41c)$$

$$N_{FF} = \frac{D_2\omega}{\left(\omega\theta_{nf} + 1\right)}\left[\cosh^2(SY_1) - 2\cosh(SY)\cosh(SY_1) + \cosh(2SY)\right] \qquad 0 \le Y < Y_1 \qquad (41d)$$

$$N_{DI} = \frac{\varphi}{\Phi}\left[\xi^2\left(\frac{\partial\Phi}{\partial X}\right)^2 + \left(\frac{\partial\Phi}{\partial Y}\right)^2\right] + \frac{\varphi\omega}{\left(\omega\theta_{nf} + 1\right)}\left[\xi^2\left(\frac{\partial\Phi}{\partial X}\right)\left(\frac{\partial\theta_{nf}}{\partial X}\right) + \left(\frac{\partial\Phi}{\partial Y}\right)\left(\frac{\partial\theta_{nf}}{\partial Y}\right)\right] \qquad 0 \le Y < Y_1 \qquad (41e)$$

To facilitate the study of entropy generation and compare the contributions from different sources of irreversibility, the equations for the nanofluid and the solid phases of the porous medium are separated. This provides the following equations for the irreversibility of heat transfer in the system.

$$N_{s,ht} = \frac{\omega^2}{(\omega\theta_s + 1)^2}\left[\xi^2\left(\frac{\partial\theta_s}{\partial X}\right)^2 + \left(\frac{\partial\theta_s}{\partial Y}\right)^2\right], \tag{42a}$$

$$N_{nf,ht} = \frac{k\ \omega^2}{\left(\omega\theta_{nf} + 1\right)^2}\left[\xi^2\left(\frac{\partial\theta_{nf}}{\partial X}\right)^2 + \left(\frac{\partial\theta_{nf}}{\partial Y}\right)^2\right]. \tag{42b}$$

By adding the components of Eqs. (41b) and (41c) the inter-phase volumetric entropy generation term can be expressed by,

$$N_{int} = \frac{Bi\ \omega^2\left(\theta_{nf} - \theta_s\right)^2}{(\omega\theta_s + 1)\left(\omega\theta_{nf} + 1\right)}. \tag{43}$$

The volumetric entropy generations for the porous insert, N_{pm} is simply the sum of the equations that are applicable to the porous medium. This is a function defining the entropy generation for the combined processes of heat transfer, viscous dissipation, and concentration gradients for any given points (X, Y).

$$N_{pm} = N_{s,ht} + N_{nf,ht} + N_{int} + N_{FF} + N_{DI}. \tag{44}$$

To calculate the total entropy generation, the sum of the parts of volumetric entropy generation is integrated over the volume of the microchannel with the inclusion of contributions from the walls. This yields a numerical value for the total entropy and is obtained by the following equation:

$$N_{Tot} = 2\int_0^1 \int_0^1 \sum N_i \, dXdY, \qquad i = w, s, nf, FF, DI. \tag{45}$$

4. Results and Discussion

This section is divided into three subsections. The first subsection illustrates the effects of various parameters such as radiation parameter and thermal conductivity ratio on the temperature fields of the solid and nanofluid phases and Nusselt number. The second subsection provides information on the influences of Damköhler number and thickness of the wall on the concentration field. The third subsection discusses the local and total entropy generation rates within the microchannel. Table 1 shows the default values of the parameters used throughout this section. To ensure about the correctness of the present solution procedure, it has been validated against that provided by Ting et al. [35] in Appendix C. This involves reducing the wall thicknesses to zero and ignoring thermal radiation and mass transfer.

4.1. Temperature fields and Nusselt number

Figure 2 shows the effects of widening the porous microchannel on the dimensionless temperature contours of the nanofluid (left column) and porous solid (right column) phases. It should be noted that in this figure, and also in other figures of this section, the walls have been excluded and only the interior part of the microchannel is depicted. As Fig. 1 indicates, increasing the non-dimensional parameter $Y_1 = \frac{h_1}{h_2}$ leads to decreasing the wall thickness and hence widening the microchannel. It is also recalled that here the dimensionless temperature has been defined on the basis of the inlet wall temperature (see Eq. (8)). Therefore, the numerical value of the temperature can vary from a negative quantity to a positive value. The internal heat generation due to nanofluid friction and the heat flux boundary condition imposed on the walls are the reasons for increasing the temperature to a positive value. Figure 2 shows that variations in the width of the microchannel impart significant effects upon the temperature fields. For instance, a comparison between Figs. 2a and 2c shows that for a fixed point inside the microchannel increasing Y_1 results in decreasing the absolute value of the dimensionless temperature of nanofluid. The same trend is observed in the non-dimensional temperature of the porous solid shown in Figs. 2b, 2d and 2f. This behaviour can be explained physically. The wall acts as a thermal resistance against the transfer of heat from the external surface of the reactor. It follows that in the current isoflux system, decreasing the wall thickness reduces

the required temperature difference for the transfer of a fixed heat flux. By comparing the left and right columns in Fig. 2, it is also seen that decreasing the wall thickness of the microchannel reduces the temperature difference between the solid and nanofluid phases. This is an important observation and implies that utilisation of LTNE model is an essential necessity in thick wall microchannels. It is further in keeping with the earlier one dimensional findings [42] and extends those to the current two-dimensional configuration. Furthermore, it is clear in Fig. 2 that the solid and nanofluid temperatures increase along the microchannel due to the internal heat generation resulting from nanofluid friction and absorption of external heat flux.

Figure 3 demonstrates the impact of thermal conductivity ratio, k, on the temperature of nanofluid and porous solid phases when the values of other thermophysical parameters are kept constant. This figure shows that as the thermal conductivity ratio increases, the magnitude of the dimensionless temperature contours in both porous solid and nanofluid phases decreases. This behaviour has been also reported in the previous investigations of forced convection of nanofluids in porous media [28,33]. It can be attributed to the fact that increasing the thermal conductivity of nanofluid enables the nanofluid phase of the system to absorb more heat from the solid component of the porous medium. Nevertheless, Fig. 3 does not imply that increasing the thermal conductivity ratio can majorly affect the temperature difference between the solid and fluid phases temperature.

The effects of radiation parameter on the temperature contours in the solid and nanofluid phases have been shown in Fig. 4. Figures 4a and 4b correspond to the microchannel without radiation effect and Figs. 4e and 4f represent a case with $Rd=2$. It is seen that augmenting the radiation parameter, increases the heat absorption by the solid phase of the porous medium from the walls. Hence, the temperature of the solid phase increases, while the temperature of the nanofluid phase decreases.

Figure 5 illustrates the effects of radiation parameter and wall thickness of the microchannel on the Nusselt number. As shown in Fig. 4, increasing the radiation parameter reduces the temperature of the nanofluid, and hence increases the ability of the nanofluid to convect the heat from the surface of the wall. Therefore increasing the radiation parameter magnifies the Nusselt number as depicted in Fig. 5a. However, Fig. 5b indicates that when the dimensionless wall thickness of the microchannel is more than 0.5, increasing the radiation parameter has only a marginal effect on the value of Nusselt number. Both Figs. 5a and 5b show that decreasing the wall thickness increases the Nusselt number. As already shown in Fig. 2,

this is due to the fact that through reducing the wall thickness the nanofluid dimensionless temperature within the microchannel decreases.

4.2. Concentration profiles

Figures 6 and 7 illustrate the effects of Damköhler number and wall thickness on the concentration field within the porous section of the microchannel. Figure 6 shows the dimensionless concentration contours for the entire length of the microchannel (Fig. 6a) and for the second half of the microchannel with different values of Damköhler numbers (Figs. 6b, c, d). A comparison between Figs. 6b to 6d reveals that decreasing the value of Damköhler number smoothen the concentration field and makes it more uniform. This is to be expected and is because of the fact that Damköhler number is directly related to the chemical reaction rate. Hence, decreasing Damköhler number represents weakening of the homogenous reaction and production of the species.

Figure 7 shows the effects of wall thickness on the concentration distribution. Examination of Figs. 7b to 7d confirms that decreasing the wall thickness of the microreactor reduces the numerical values of the dimensionless concentration contours. As already discussed, reducing the wall thickness of the microchannel decreases the temperature of the nanofluid phase and subsequently affects the concentration field through thermal diffusion effect. Although not shown here the impact of radiation parameter on the concentration field is quite marginal. Radiation affects the temperature field to some extent but only the second derivative of temperature appears in the mass transfer Eq. (46). This smears out the effects of thermal radiation and renders the concentration field rather indifferent to variation in radiation parameter.

Figures 6 and 7 further show that due to the axial advection and production, the species are washed away from the entrance of the channel. Thus, in moving from the entrance of the microreactor towards the exist plane, the dimensionless concentration is constantly increasing. Further, the concentration of species appears to be higher in the vicinity of the walls of microreactor compared to that on the centreline. As the nanofluid temperature near the wall is always higher than the temperature around the centre of the microchannel, the thermo-diffusion effects generate the observed transversal gradient in the species field.

4.3. Entropy generation and performance evaluation criterion

Figures 8-12 illustrate the effects of different thermophysical parameters on the local and total entropy generation rate within the microreactor. In all of the local entropy generation illustrations in this section, the contributions from different sources of irreversibility are shown in subfigure *a* to *e*, and the overall local entropy generation is plotted in sub-figure *f*. Figure 8 shows the local entropy generation for the porous

section of the microreactor calculated for the default values given in Table 1. This provides a basis to compare the effects of different parameters. Through a simple comparison between the different sources of irreversibility, it is clear that the diffusive irreversibility is the main source of entropy generation and is followed by that of nanofluid friction. It is also observed that the solid and nanofluid entropy generation rates are smaller around the centre of the microreactor. However, the inter-phase volumetric entropy generation rate is larger at the centreline. Figure 8d further indicates that by moving transversally from the walls of the reactor towards the centreline, the local entropy generation by nanofluid friction first decreases. It then reaches a minimum value and again hits a high value at the centre of the microreactor.

The entropic effects of Sort and Damköhler numbers are further analysed in Fig. 9. In this figure, the values of Soret and Damköhler number were reduced to 0.01 and 0.3 respectively, which represent a significant reduction in comparison to their default values shown in Table 1 and used in Fig. 8. A comparison between Figs. 8e and 9a reveals that by decreasing the numerical value of Soret number from 0.7 to 0.01 the mass transfer irreversibility decreases by about 40%. Yet, reduction of Damköhler number from 1 (in Fig. 8e) to 0.3 (in Fig. 9c) results in 75% reduction in the mass transfer irreversibility. A very similar reduction in overall entropy generation can be seen in Figs. 9b and 9d in comparison with Fig. 8f. As already discussed this is due to the fact that irreversibility of the process is dominated by the entropy generation through mass transfer. Figure 9 clearly shows that while both Soret and Damköhler number are rather influential in determining the irreversibility of the process, Damköhler number seems to be of higher significance.

Figure 10 depicts the effects of varying the wall thickness on the local entropy generation rates. This figure shows that increasing the thickness of the wall through changing the value of Y_1 from 0.8 to 0.6 has a marginal effect on the nanofluid friction part of the entropy generation. However, it drastically increases the entropy generation by mass transfer. Comparing the values of overall entropy generation rates in Figs. 8 and 10 shows that increasing the thickness of the microchannel wall by two times, has increased the entropy generation rate by almost tenfold. This is a very important result and clearly demonstrates the significance of wall thickness in the level of irreversibility encountered within the microreactor.

Figure 11 illustrates variations of the total entropy generation rate versus radiation parameter, and Soret and Damköhler numbers. This figure shows that, as expected, increasing either of Soret or Damköhler number would increase the total entropy generation within the microreactor. It also shows that increasing the radiation parameter leads to the reduction of the total entropy generated in the system. Strengthening

the thermal radiation intensifies the internal heat exchanges between the components of the reactor and hence leads to smaller temperature gradients. This tends to suppress the thermal and mass transfer irreversibilities and therefore reduces the total entropy generation of the reactor. Figure 11 further shows an interesting relation between the radiation parameter and total entropy in which initial increases of radiation parameter from zero result in noticeable reduction in the total entropy. However, further increase in the radiation parameter causes only minor decreases of the total entropy. Increasing the values of Sort and Damköhler numbers widens the range over which the total entropy is affected by thermal radiation.

The combined effects of wall thickness and Soret and Damköhler numbers upon the total entropy generation are illustrated by Fig. 12. This figure clearly shows that regardless of the values of Soret and Damköhler numbers reducing the wall thickness (i.e., increasing Y_1) causes substantial decreases in the total irreversibility of the system. Figure 12 further shows that such reduction features a highly nonlinear relation with Y_1. It is also clear that total entropy generation in thick wall microreactor is majorly dependent upon the Damköhler number and is affected by Soret number to a lesser extent. For instance, at Y_1=0.5 by increasing the value of Damköhler number from 0.8 to 1.2, the value of the total entropy generation grows for nearly 80%. However, this influence decreases sharply as the wall becomes thinner.

5. Conclusions

A porous microreactor accommodating a homogenous chemical reaction and featuring thick walls was investigated. The axisymmetric system was subject to thermal load in the form of constant heat flux. Two-dimensional convection of heat together with the conjugate heat transfer in the walls was tackled analytically. This included the internal generation of heat through viscous dissipation of flow kinetic energy. Further, a two-dimensional advection-diffusion-reaction model with zeroth order chemical reaction was employed to represent the production and transfer of the chemical species. This was coupled to the transport of heat through thermal diffusion of mass. The resultant coupled heat and mass transfer problem was solved analytically. The calculated temperature and concentration fields were then used to predict the local and total entropy generation within the microreactor. The main findings of this study can be summarised as follows.

- Decreasing thicknesses of the microreactor walls, provides more uniform temperature distribution within both solid and nanofluid phases of the system.

- Increasing the radiation parameter, increases the solid phase temperature and decreases the nanofluid phase temperature. This causes a decrease in the total entropy generation of the microreactor.
- As the dimensionless temperature of the nanofluid decreases by increasing the radiation parameter, the nanofluid gains more power to wash away heat from the surface of the walls and hence the Nusselt number increases.
- Increasing Damköhler and Soret numbers intensifies the concentration of species, and magnifies the mass transfer component of the entropy generation rate.
- In general, the mass transfer part of the entropy generation dominants exergy destruction within the microreactor, although depending on the numerical values of other parameters the nanofluid friction part of the entropy generation can be of comparable significance.
- The total irreversibility appears to be strongly dependent upon the wall thickness and is also affected by the moderate values of radiation parameter.

Acknowledgment

Graeme Hunt gratefully acknowledges the financial support of the University of Glasgow through EPSRC DTA (G. Hunt) funding award number EP/M506539/1. Nader Karimi acknowledges the partial financial support by EPSRC through grant number EP/N020472/1 (Thermal-pump) and Lilian Govone would like to thank the financial support provided through the Erasmus programme.

Appendix A: Nanofluid thermo-physical properties

Following Brinkman [43], the effective viscosity for a nanofluid is modelled as a dilute suspension of small rigid spheres in a base fluid,

$$\mu_{nf} = \frac{\mu_f}{(1-\phi)^{2.5}}. \tag{A1}$$

The ratio of the effective thermal conductivity of the nanofluid to the thermal conductivity of the base fluid allows the former to be approximated using the Maxwell-Garnetts model [44].

$$\frac{k_{nf}}{k_f} = \frac{k_p + 2k_f - 2\phi(k_f - k_p)}{k_p + 2k_f + \phi(k_f - k_p)}, \tag{A2}$$

while the effective density and specific heat are defined as follows [44].

$$\rho_{nf} = \rho_f(1-\phi) + \rho_p, \tag{A3a}$$

$$(\rho C_p)_{nf} = \left(\rho C_p\right)_f (1-\phi) + \left(\rho C_p\right)_p \phi. \tag{A3b}$$

Appendix B: Closed form constants

Provided here is a list of the closed form constants $D_1 - D_4$, $E_1 - E_{12}$, and $F_1 - F_5$:

$$D_1 = \frac{SY_1}{SY_1\cosh(SY_1) - \sinh(SY_1)} \tag{B1a}$$

$$D_2 = Br' D_1^2 S^2 \tag{B1b}$$

$$D_3 = \frac{D_1}{Y_1} - D_2\cosh(SY_1) \tag{B1c}$$

$$D_4 = -\frac{D_1}{Y_1}\cosh(SY_1). \tag{B1d}$$

$$E_1 = \frac{-Y_1}{k_{e1}}, \qquad E_2 = \frac{1}{k_{e1}}, \tag{B2a,b}$$

$$E_3 = \frac{BiD_2 - 4D_2S^2 - 4BiD2S^2Rd}{16k(1+Rd)S^4 - 4k(1+Rd)S^2\alpha^2}, \qquad E_4 = \frac{BiD_3 - D_3S^2}{k(1+Rd)S^4 - k(1+Rd)S^2\alpha^2}, \tag{B2c,d}$$

$$E_5 = \frac{-[D_4 + 2E_6k + (D_3 + E_4kS^2)\cosh(SY_1) + (D_2 + 4E_3kS^2)\cosh(2SY_1)]\mathrm{sech}(\alpha Y_1)}{k\alpha^2}, \tag{B2e}$$

$$E_6 = \frac{-BiD_4}{2k(1+Rd)\alpha^2}, \qquad E_7 = 0, \tag{B2f,g}$$

$$\begin{aligned} E_8 = \frac{1}{2k(1+Rd)\alpha^2}\big[&2D_4 + 2E_6k(1+Rd)(2 - Y_1^2\alpha^2) \\ &+ 2\big(D_3 + E_4k(1+Rd)(S^2 - \alpha^2)\big)\cosh(SY_1) \\ &+ 2\big(D_4 + E_3k(1+Rd)(4S^2 - \alpha^2)\big)\cosh(2SY_1)\big], \end{aligned} \tag{B2h}$$

$$E_9 = \frac{BiD_2}{16k(1+Rd)S^4 - 4k(1+Rd)S^2\alpha^2}, \qquad E_{10} = \frac{BiD_3}{k(1+Rd)S^4 - k(1+Rd)S^2\alpha^2}, \tag{B2i,j}$$

$$E_{11} = \frac{-[2E_6 + E_{10}S^2\cosh(SY_1) + 4E_9S^2\cosh(2SY_1)]\mathrm{sech}(\alpha Y_1)}{\alpha^2}, \tag{B2k}$$

$$E_{12} = \frac{1}{2\alpha^2}[4E_6 - 2E_6Y_1^2\alpha^2 + 2E_{10}(S^2 - \alpha^2)\cosh(SY_1) + 2E_9(4S^2 - \alpha^2)\cosh(2SY_1)], \tag{B2l}$$

$$F_1 = \frac{D_2k(Bi - 4(1+Rd)S^2)Sr}{4S^2Y_1\varepsilon(-Bi(1+k+Rd) + 4k(1+Rd)S^2)} \tag{B22}$$

$$F_2 = \frac{D_3k(Bi - (1+Rd)S^2)Sr}{S^2Y_1\varepsilon(-Bi(1+k+Rd) + k(1+Rd)S^2)} - \frac{\gamma}{SY_1^2(SY_1\cosh(SY_1) - \sinh(SY_1))} \tag{B23}$$

$$F_3 = \frac{E_5kSr}{Y_1\varepsilon} \tag{B24}$$

$$F_4 = -\frac{D_4kSr}{2Y_1\varepsilon(1+k+Rd)} - \frac{\gamma(S(Y_1 - 1)\cosh(SY_1) - \sinh(SY_1))}{2Y_1^2(SY_1\cosh(SY_1) - \sinh(SY_1))} \tag{B25}$$

$$F_5 = \frac{E_8 kSr}{Y_1 \varepsilon} + \frac{\left(2\gamma + S^2 Y_1^2 (Y_1(2+\gamma) - \gamma)\right)\cosh(SY_1) - SY_1^2(2+\gamma)\sinh(SY_1)}{2SY_1^2(SY_1\cosh(SY_1) - \sinh(SY_1))} \tag{B26}$$

$$- \frac{kSr}{Y_1 \varepsilon}\left[E_8 - \frac{D_4 Y_1^2}{2(1+k+Rd)} + \frac{D_3(Bi - (1+Rd)S^2)\cosh(SY_1)}{S^2(-Bi(1+k+Rd) + k(1+Rd)S^2)}\right.$$

$$\left. + \frac{D_2(Bi - 4(1+Rd)S^2)\cosh(2SY_1)}{4S^2(-Bi(1+k+Rd) + 4k(1+Rd)S^2)} + E_5\cosh(\alpha Y_1)\right]$$

Appendix C: Validation

To validate the mathematical model developed in Sections 2-3, it is demonstrated here that when the wall thickness and thermal radiation tend to zero, the analytical form of the temperature fields reduce to those presented by Ting et al. [35] with no internal heat generation term. To produce a system equivalent to that of Ref. [35], we set $h_1 = h_2$, $q = 0$ and $q_1'' = q_2''$. That is in terms of non-dimensional parameters; $Y_1 = 1$, $Rd = 0, Q = 1$ and also $q_{gen}''' = 0$, which renders $\Omega_{gen} = 0$. The momentum Eqs. (11)-(13) can clearly be seen to reduce to the corresponding equations.

By utilising the above parameters Eq. (17) become,

$$\frac{d\bar{T}_{nf}}{dx} = \frac{1}{\rho_{nf} C_{p,nf} \bar{u} h_2^2}\left[h_2 q_1'' + \frac{\mu_{eff} S^3 \bar{u}^2 \cosh(S)}{S\cosh(S) - \sinh(S)}\right] = \Omega_T. \tag{C1}$$

Next, the radial thermal equations can be determined from Eqs. (19b) and (19c) using the given conditions to yield the coupled equations:

$$k\theta_{nf}'' + Bi\left(\theta_s - \theta_{nf}\right) + D_2' cosh(2SY) + D_3'\cosh(SY) + D_4' = 0, \qquad 0 \le Y < 1 \tag{C2a}$$

$$\theta_s'' - Bi\left(\theta_s - \theta_{nf}\right) = 0, \qquad 0 \le Y < 1 \tag{C2b}$$

where the modified coefficients (which are shown by use of a prime) are:

$$D_1' = \frac{S}{S\cosh(S) - \sinh(S)} \tag{C3a}$$

$$D_2' = Br' D_1'^2 S^2 \tag{C3b}$$

$$D_3' = D_1' - D_2'\cosh(S) \tag{C3c}$$

$$D_4' = -D_1'\cosh(S) \tag{C3d}$$

The coefficients $D_1' - D_4'$ are the same as those calculated by Ting et al. for the coupled thermal equations investigated therein under the previously stated conditions. Thus, it follows that the final nanofluid and porous solid thermal equations, Eqs. (22b) and (22c) may be reproduced as follows.

$$\theta_{nf}(Y) = E_3'\cosh(2SY) + E_4'\cosh(SY) + E_5'\cosh(\alpha Y) + E_6' Y^2 + E_7' Y + E_8' \qquad 0 \le Y < 1 \tag{C4a}$$

$$\theta_s(Y) = E_9'\cosh(2SY) + E_{10}'\cosh(SY) + E_{11}'\cosh(\alpha Y) + E_6' Y^2 + E_7' Y + E_{12}' \qquad 0 \le Y < 1 \tag{C4b}$$

where the new coefficients are defined as:

$$E_3' = \frac{D_2'(4S^2 - Bi)}{4S^2(-4kS^2 + Bik + Bi)}, \qquad E_4' = \frac{D_3'(S^2 - Bi)}{S^2(k\alpha^2 - kS^2)}, \tag{C5a,b}$$

$$E_5' = \frac{-[D_4' + 2E_6'k + (D_3' + E_4'kS^2)\cosh(S) + (D_2' + 4E_3'kS^2)\cosh(2S)]\mathrm{sech}(\alpha)}{Bi(k+1)}, \tag{C5c}$$

$$E_6' = \frac{-D_4'}{2(k+1)}, \qquad E_7' = 0, \tag{C5d,e}$$

$$E_8' = \frac{1}{2k\alpha^2}\big[2D_4' + 2E_6'k(2-\alpha^2) + 2\big(D_3' + E_4'k(S^2-\alpha^2)\big)\cosh(S) + 2\big(D_4' + E_3'k(4S^2-\alpha^2)\big)\cosh(2S)\big], \tag{C5f}$$

$$E_9' = \frac{BiE_3'}{Bi - 4S^2}, \qquad E_{10}' = \frac{BiE_4'}{Bi - S^2}, \tag{C5g,h}$$

$$E_{11}' = \frac{-[2E_6' + E_{10}'S^2\cosh(S) + 4E_9'S^2\cosh(2S)]\mathrm{sech}(\alpha)}{\alpha^2}, \tag{C5i}$$

$$E_{12}' = \frac{1}{2\alpha^2}[4E_6' - 2E_6'\alpha^2 + 2E_{10}'(S^2-\alpha^2)\cosh(S) + 2E_9'(4S^2-\alpha^2)\cosh(2S)], \tag{C5j}$$

With the appropriate rearranging of terms, the above coefficients indicate that Eqs. (C4a) and (C4b) are analytically identical to the nanofluid and porous solid thermal equations in the work by Ting et al. [35] with a temperature at the upper wall equal to 0 due to the equality of the external heat flux at the bottom and top walls.

References

[1] Hessel V, Renken A, Schouten JC, Yoshida JI. Micro Process Engineering: A Comprehensive Handbook. vol. 1. 2013. doi:10.1002/9783527631445.

[2] Hessel V, Hardt S, Löwe H. Chemical Micro Process Engineering: Fundamentals, Modelling and Reactions. 2004. doi:10.1002/3527603042.fmatter.

[3] Yao X, Zhang Y, Du L, Liu J, Yao J. Review of the applications of microreactors. Renew Sustain Energy Rev 2015;47:519–39. doi:10.1016/j.rser.2015.03.078.

[4] Kolb G. Review: Microstructured reactors for distributed and renewable production of fuels and electrical energy. Chem Eng Process Process Intensif 2013;65:1–44. doi:10.1016/j.cep.2012.10.015.

[5] Yao F, Chen Y, Peterson GP. Hydrogen production by methanol steam reforming in a disc microreactor with tree-shaped flow architectures. Int J Heat Mass Transf 2013;64:418–25. doi:10.1016/j.ijheatmasstransfer.2013.04.057.

[6] Kück a, Steinfeldt M, Prenzel K, Swiderek P, Gleich a V, Thöming J. Green nanoparticle production

using micro reactor technology. J Phys Conf Ser 2011;304:12074. doi:10.1088/1742-6596/304/1/012074.

[7] Roberge DM, Ducry L, Bieler N, Cretton P, Zimmermann B. Microreactor technology: A revolution for the fine chemical and pharmaceutical industries? Chem Eng Technol 2005;28:318–23. doi:10.1002/ceat.200407128.

[8] Tanimu A, Jaenicke S, Alhooshani K. Heterogeneous catalysis in continuous flow microreactors: A review of methods and applications. Chem Eng J 2017;327:792–821. doi:10.1016/j.cej.2017.06.161.

[9] Rebrov E V., Schouten JC, de Croon MHJM. Single-phase fluid flow distribution and heat transfer in microstructured reactors. Chem Eng Sci 2011;66:1374–93. doi:10.1016/j.ces.2010.05.044.

[10] Kolb G, Hessel V. Micro-structured reactors for gas phase reactions. Chem Eng J 2004;98:1–38. doi:10.1016/j.cej.2003.10.005.

[11] Hunt G, Karimi N, Torabi M. Analytical investigation of heat transfer and classical entropy generation in microreactors - The influences of exothermicity and asymmetry. Appl Therm Eng 2017;119:403–24. doi:10.1016/j.applthermaleng.2017.03.057.

[12] Elliott A, Torabi M, Karimi N. Thermodynamics analyses of porous microchannels with asymmetric thick walls and exothermicity: An entropic model of microreactors. J Therm Sci Eng Appl 2017;9:41013. doi:10.1115/1.4036802.

[13] Torabi M, Torabi M, Peterson GP. Entropy generation of double diffusive forced convection in porous channels with thick walls and Soret effect. Entropy 2017;19:171. doi:10.3390/e19040171.

[14] Delsman ER, de Croon MHJM, Elzinga GD, Cobden PD, Kramer GJ, Schouten JC. The influence of differences between microchannels on microreactor performance. Chem Eng Technol 2005;28:367–75. doi:10.1002/ceat.200407126.

[15] Li J, Chou SK, Li ZW, Yang WM. Experimental investigation of porous media combustion in a planar micro-combustor. Fuel 2010;89:708–15. doi:10.1016/j.fuel.2009.06.026.

[16] Torabi M, Karimi N, Peterson GP, Yee S. Challenges and progress on the modeling of entropy generation in porous media: A review. Int J Heat Mass Transf 2017;114:31–46. doi:http://dx.doi.org/10.1016.

[17] Namkung H, Yuan X, Lee G, Kim D, Kang TJ, Kim HT. Reaction characteristics through catalytic steam gasification with ultra clean coal char and coal. J Energy Inst 2014;87:253–62.

doi:10.1016/j.joei.2014.03.003.

[18] Elias Y, Rudolf von Rohr P, Bonrath W, Medlock J, Buss A. A porous structured reactor for hydrogenation reactions. Chem Eng Process Process Intensif 2015;95:175–85. doi:10.1016/j.cep.2015.05.012.

[19] Avril A, Hornung CH, Urban A, Fraser D, Horne M, Veder J-P, et al. Continuous flow hydrogenations using novel catalytic static mixers inside a tubular reactor. React Chem Eng 2017;2:180–8. doi:10.1039/C6RE00188B.

[20] Guettel R, Turek T. Assessment of micro-structured fixed-bed reactors for highly exothermic gas-phase reactions. Chem Eng Sci 2010;65:1644–54. doi:10.1016/j.ces.2009.11.002.

[21] Yang K, Vafai K. Analysis of temperature gradient bifurcation in porous media – An exact solution. Int J Heat Mass Transf 2010;53:4316–25. doi:10.1016/j.ijheatmasstransfer.2010.05.060.

[22] Karimi N, Agbo D, Talat Khan A, Younger PL. On the effects of exothermicity and endothermicity upon the temperature fields in a partially-filled porous channel. Int J Therm Sci 2015;96:128–48. doi:10.1016/j.ijthermalsci.2015.05.002.

[23] Ju Y, Maruta K. Microscale combustion: Technology development and fundamental research. Prog Energy Combust Sci 2011;37:669–715. doi:10.1016/j.pecs.2011.03.001.

[24] Torabi M, Zhang K. Temperature distribution, local and total entropy generation analyses in MHD porous channels with thick walls. Energy 2015;87:540–54. doi:10.1016/j.energy.2015.05.009.

[25] Wang K, Vafai K, Wang D. Analytical characterization of gaseous slip flow and heat transport through a parallel-plate microchannel with a centered porous substrate. Int J Numer Methods Heat Fluid Flow 2016;26:854–78. doi:10.1108/HFF-09-2015-0364.

[26] Ting TW, Hung YM, Guo N. Entropy generation of viscous dissipative nanofluid flow in thermal non-equilibrium porous media embedded in microchannels. Int J Heat Mass Transf 2015;81:862–77. doi:10.1016/j.ijheatmasstransfer.2014.02.041.

[27] Alazmi B, Vafai K. Constant wall heat flux boundary conditions in porous media under local thermal non-equilibrium conditions. Int J Heat Mass Transf 2002;45:3071–87.

[28] Torabi M, Dickson C, Karimi N. Theoretical investigation of entropy generation and heat transfer by forced convection of copper–water nanofluid in a porous channel — Local thermal non-equilibrium and partial filling effects. Powder Technol 2016;301:234–54. doi:10.1016/j.powtec.2016.06.017.

[29] Ting TW, Hung YM, Guo N. Entropy generation of viscous dissipative nanofluid convection in asymmetrically heated porous microchannels with solid-phase heat generation. Energy Convers Manag 2015;105:731–45. doi:10.1016/j.icheatmasstransfer.2015.09.003.

[30] Elliott A, Torabi M, Karimi N, Cunningham S. On the effects of internal heat sources upon forced convection in porous channels with asymmetric thick walls. Int Commun Heat Mass Transf 2016;73:100–10. doi:10.1016/j.icheatmasstransfer.2016.02.016.

[31] Atkins P, Paula J De. Atkins' physical chemistry. 2009. doi:10.1021/ed056pA260.1.

[32] Chaudhari R V., Ramachandran PA. Influence of Mass Transfer on Zero-Order Reaction in a Catalytic Slurry Reactor. Ind Eng Chem Fundam 1980;19:201–6. doi:10.1021/i160074a013.

[33] Dickson C, Torabi M, Karimi N. First and second law analyses of nanofluid forced convection in a partially-filled porous channel – The effects of local thermal non-equilibrium and internal heat sources. Appl Therm Eng 2016;103:459–80. doi:10.1016/j.applthermaleng.2016.04.095.

[34] Albani D, Vilé G, Beltran Toro MA, Kaufmann R, Mitchell S, Pérez-Ramírez J. Structuring hybrid palladium nanoparticles in metallic monolithic reactors for continuous-flow three-phase alkyne hydrogenation. React Chem Eng 2016;1:454–62. doi:10.1039/C6RE00114A.

[35] Ting TW, Hung YM, Guo N. Entropy generation of viscous dissipative nanofluid convection in asymmetrically heated porous microchannels with solid-phase heat generation. Energy Convers Manag 2015;105:731–45. doi:10.1016/j.enconman.2015.08.022.

[36] Modest MF. Radiative Heat Transfer. Elsevier; 2013. doi:10.1016/B978-0-12-386944-9.50022-4.

[37] Deen WM. Analysis of transport phenomena. Oxford University Press; 1998.

[38] Ho CJ, Chen DS, Yan WM, Mahian O. Buoyancy-driven flow of nanofluids in a cavity considering the Ludwig-Soret effect and sedimentation: Numerical study and experimental validation. Int J Heat Mass Transf 2014;77:684–94. doi:10.1016/j.ijheatmasstransfer.2014.05.059.

[39] Bahloul A, Boutana N, Vasseur P. Double-diffusive and Soret-induced convection in a shallow horizontal porous layer. J Fluid Mech 2003;491:325–52. doi:10.1017/S0022112003005524.

[40] Govone L, Torabi M, Hunt G, Karimi N. Non-equilibrium thermodynamic analysis of double diffusive, nanofluid forced convection in catalytic microreactors with radiation effects. Entropy 2017;19. doi:10.3390/e19120690.

[41] Matin MH, Pop I. Forced convection heat and mass transfer flow of a nanofluid through a porous channel with a first order chemical reaction on the wall. Int Commun Heat Mass Transf

2013;46:134–41. doi:10.1016/j.icheatmasstransfer.2013.05.001.

[42] Torabi M, Zhang K, Karimi N, Peterson GP. Entropy generation in thermal systems with solid structures – A concise review. Int J Heat Mass Transf 2016;97:917–31. doi:10.1016/j.ijheatmasstransfer.2016.03.007.

[43] Brinkman HC. The Viscosity of Concentrated Suspensions and Solutions. J Chem Phys 1952;20:571–571. doi:10.1063/1.1700493.

[44] Khanafer K, Vafai K, Lightstone M. Buoyancy-driven heat transfer enhancement in a two-dimensional enclosure utilizing nanofluids. Int J Heat Mass Transf 2003;46:3639–53. doi:10.1016/S0017-9310(03)00156-X.

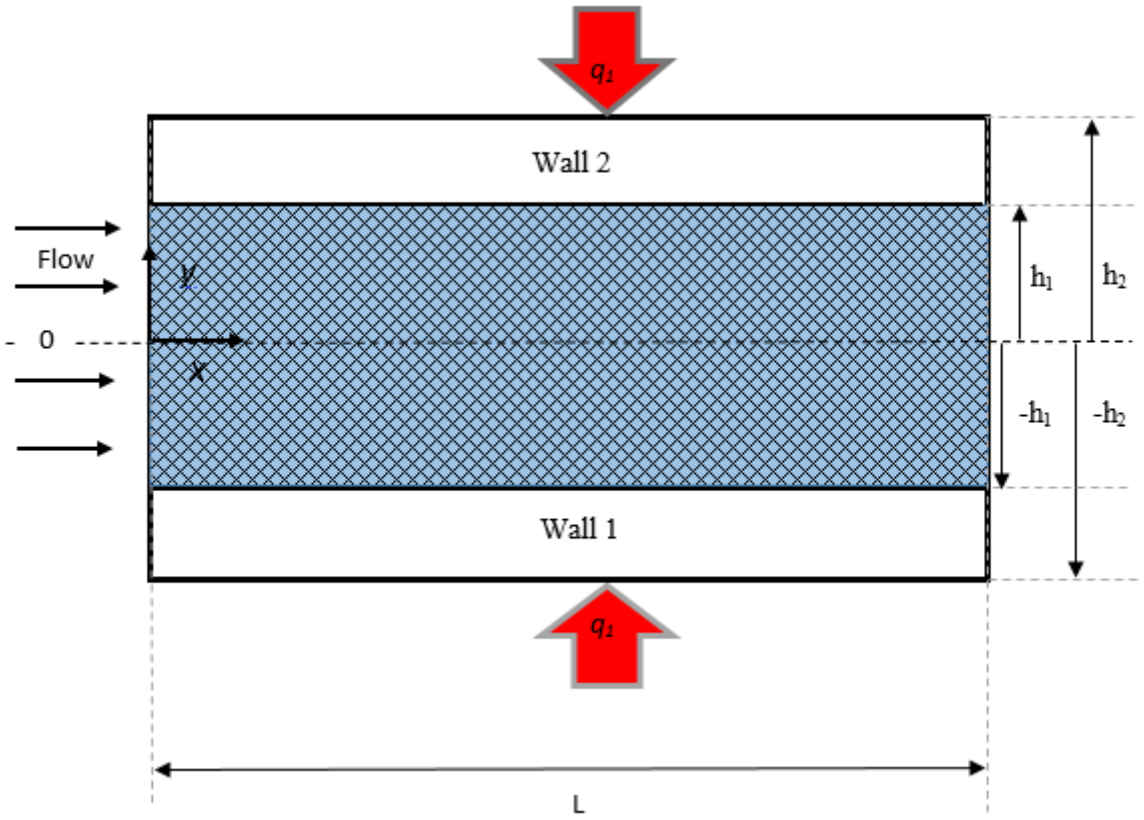

Fig. 1. Schematic view of the investigated microreactor.

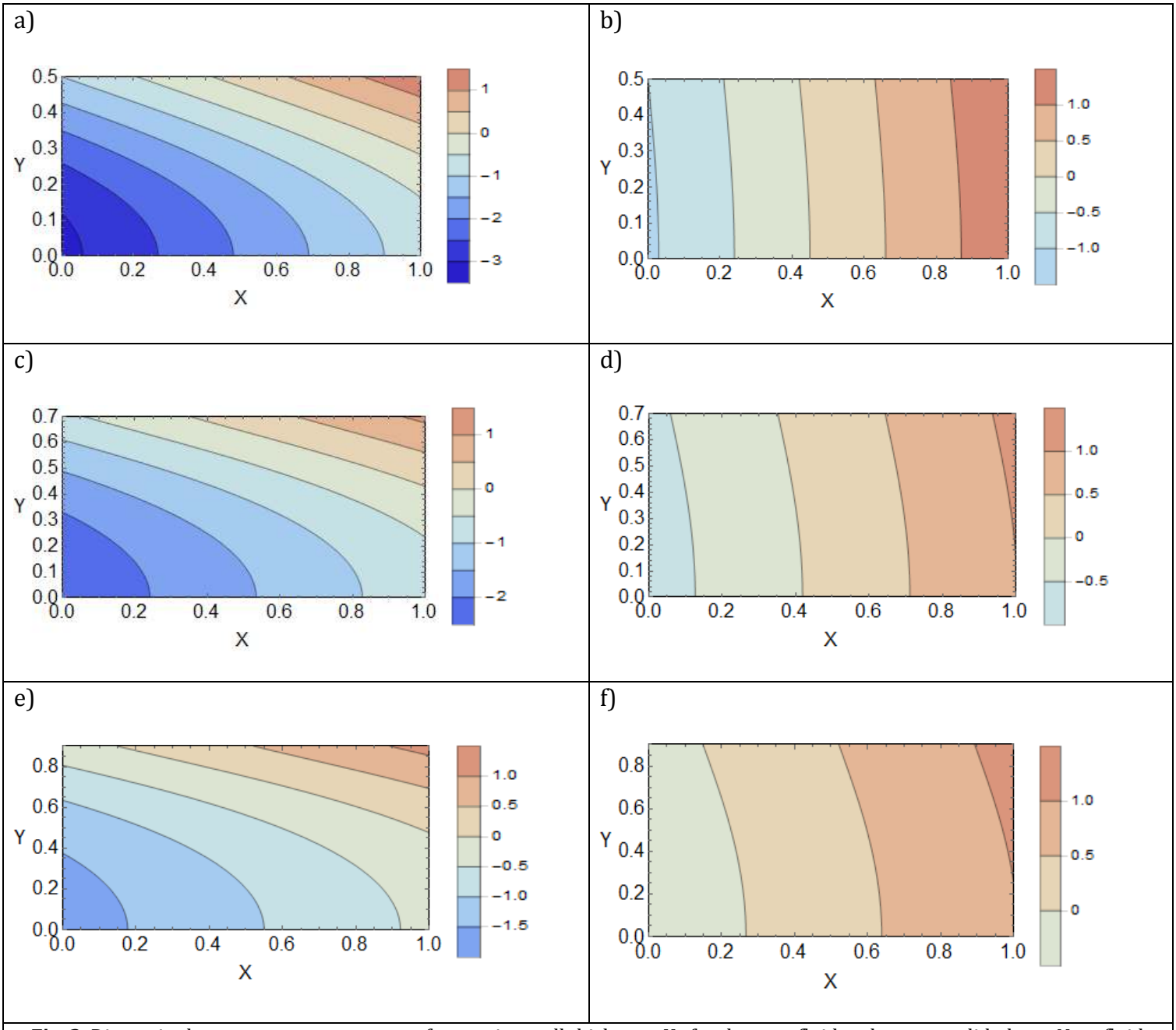

Fig. 2. Dimensionless temperature contours for varying wall thickness, Y_1, for the nanofluid and porous solid phase. Nanofluid phase is shown in a), c), and e) with Y_1 values of 0.5, 0.7 and 0.9, respectively. Porous solid phase is shown in b), d), and f) with Y_1 values of 0.5, 0.7 and 0.9 respectively.

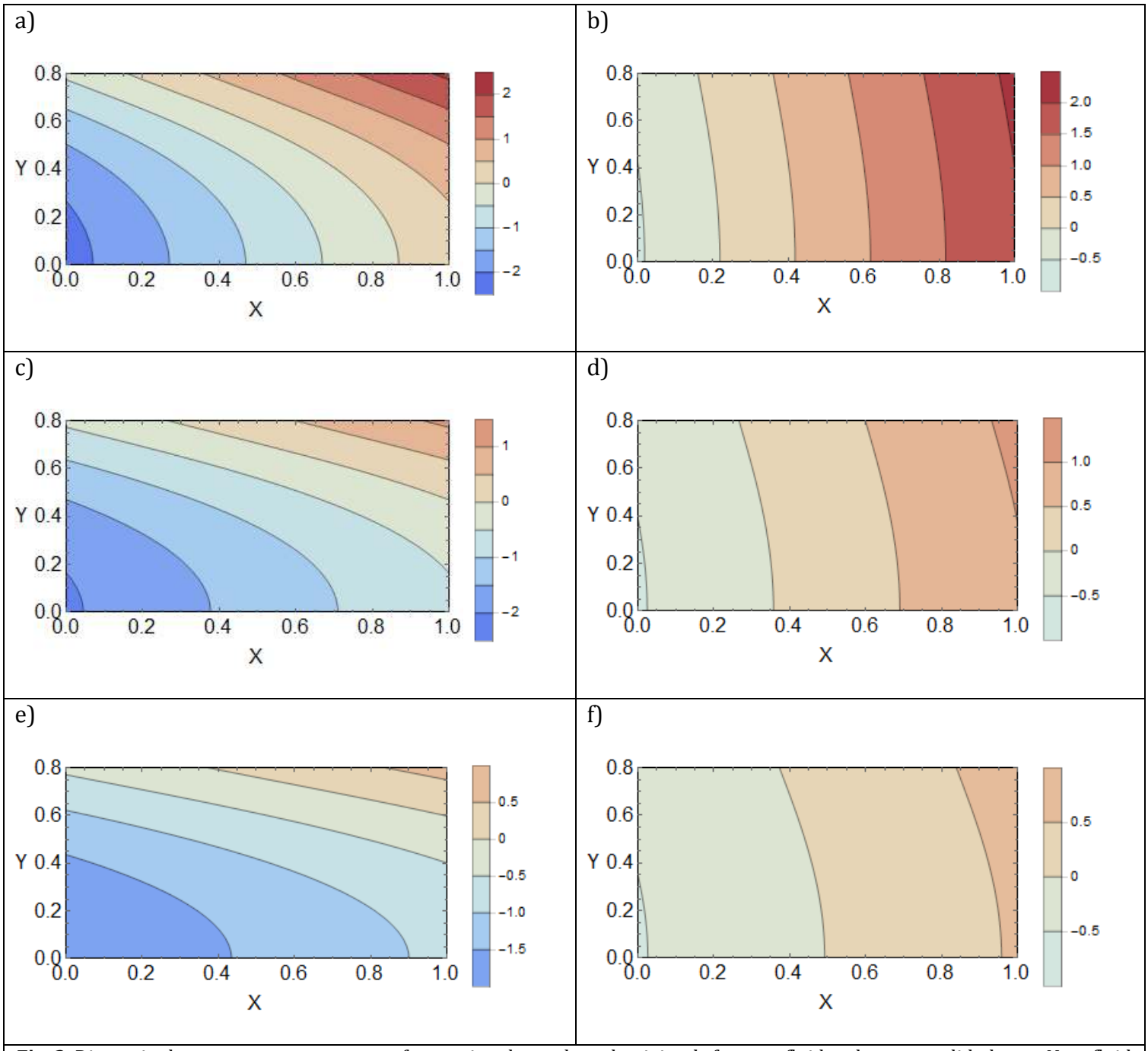

Fig. 3. Dimensionless temperature contours for varying thermal conductivity, k, for nanofluid and porous solid phases. Nanofluid phase is shown in a), c), d) and e) with k values of 0.03, 0.05, 0.07, respectively. Porous solid phase is shown in b), d), and f) with k values of 0.03, 0.05, 0.07, respectively.

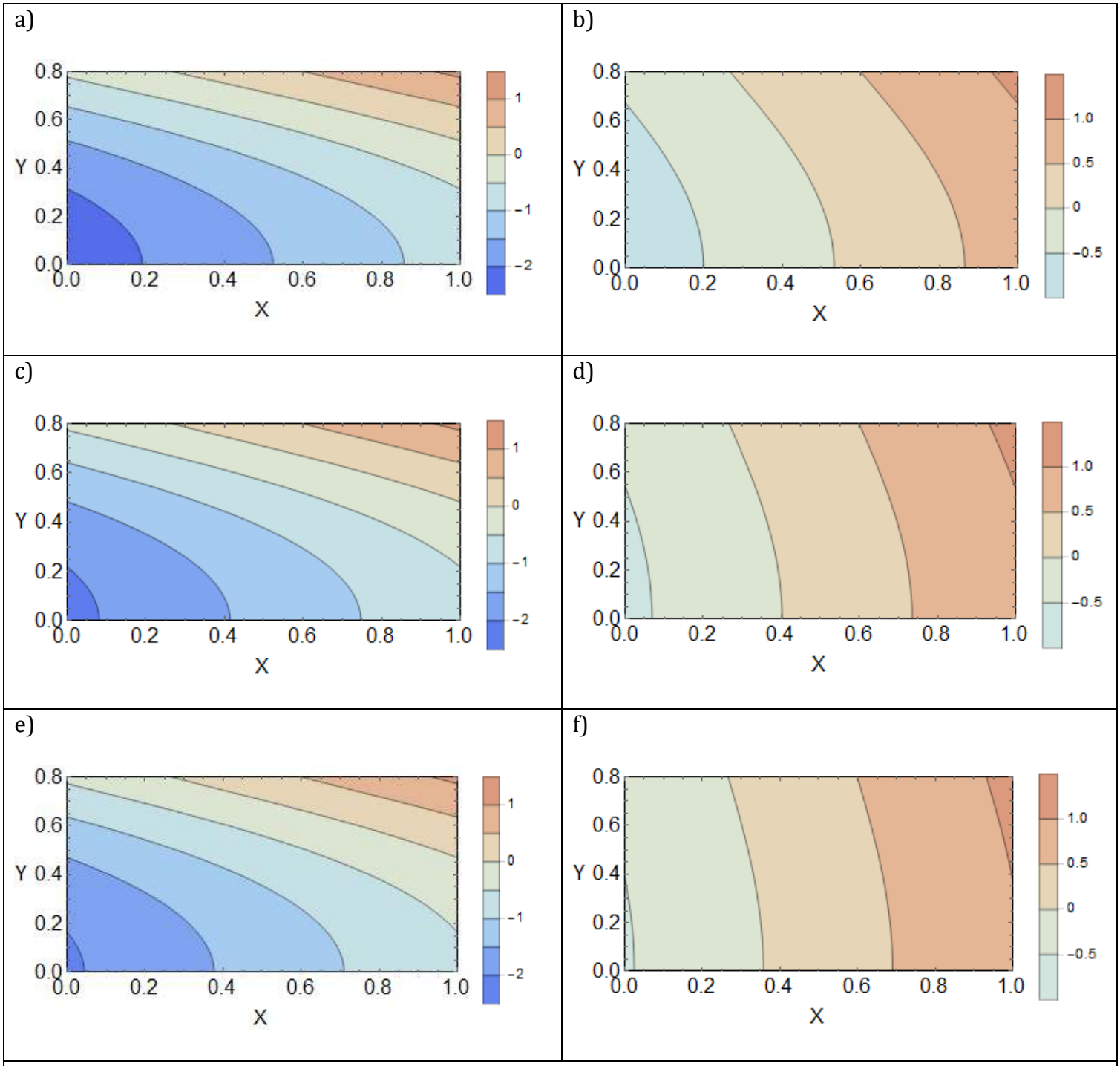

Fig. 4. Dimensionless temperature contours for varying radiation parameter, Rd, for nanofluid and porous solid phases. Nanofluid phase is shown in a), c), d) and e) with Rd values of 0, 1, 2, respectively. Porous solid phase is shown in b), d), and f) with Rd values of 0, 1, 2, respectively.

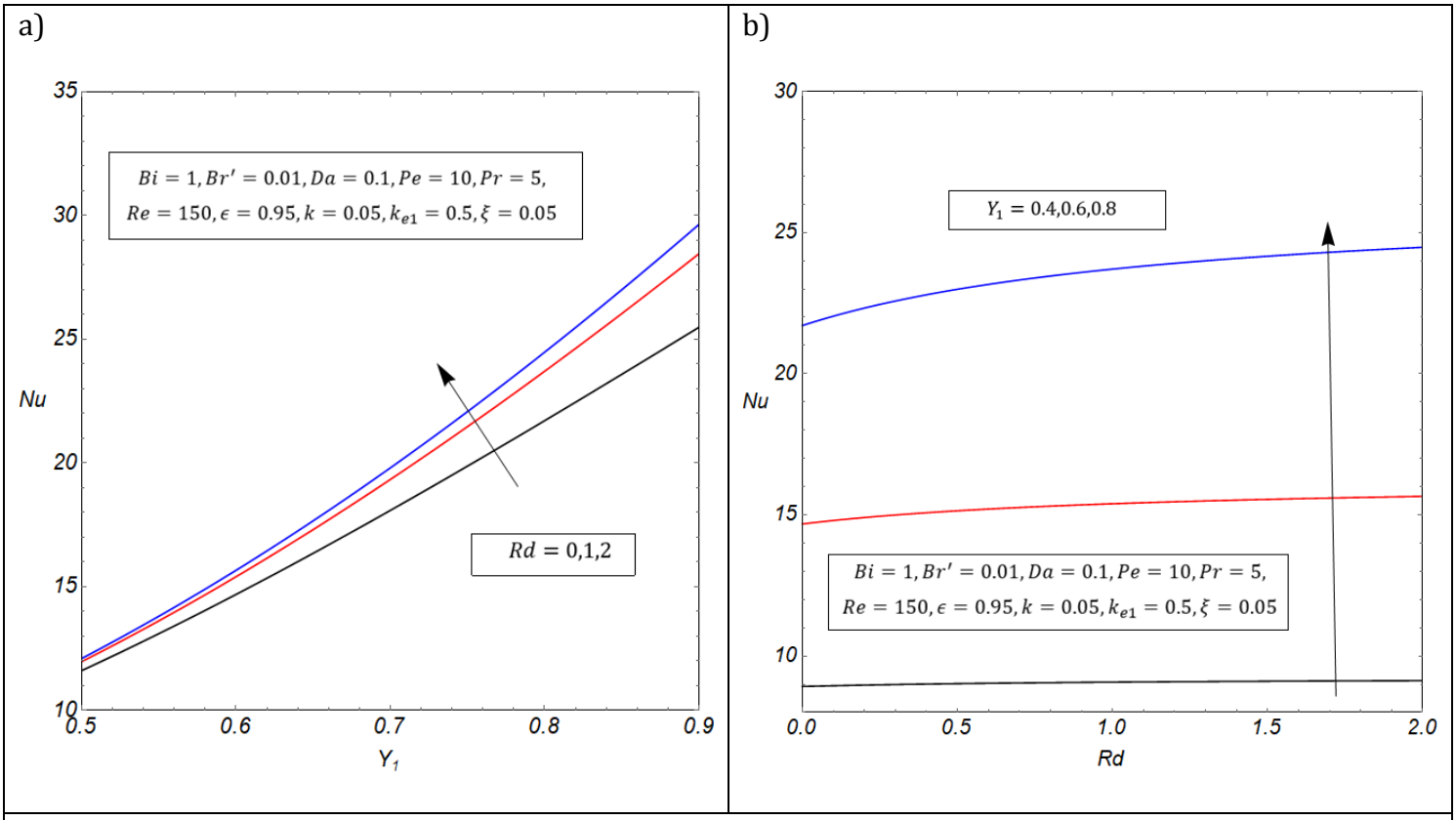

Fig. 5. Variation of Nusselt number with a) the wall thickness and b) radiation parameter.

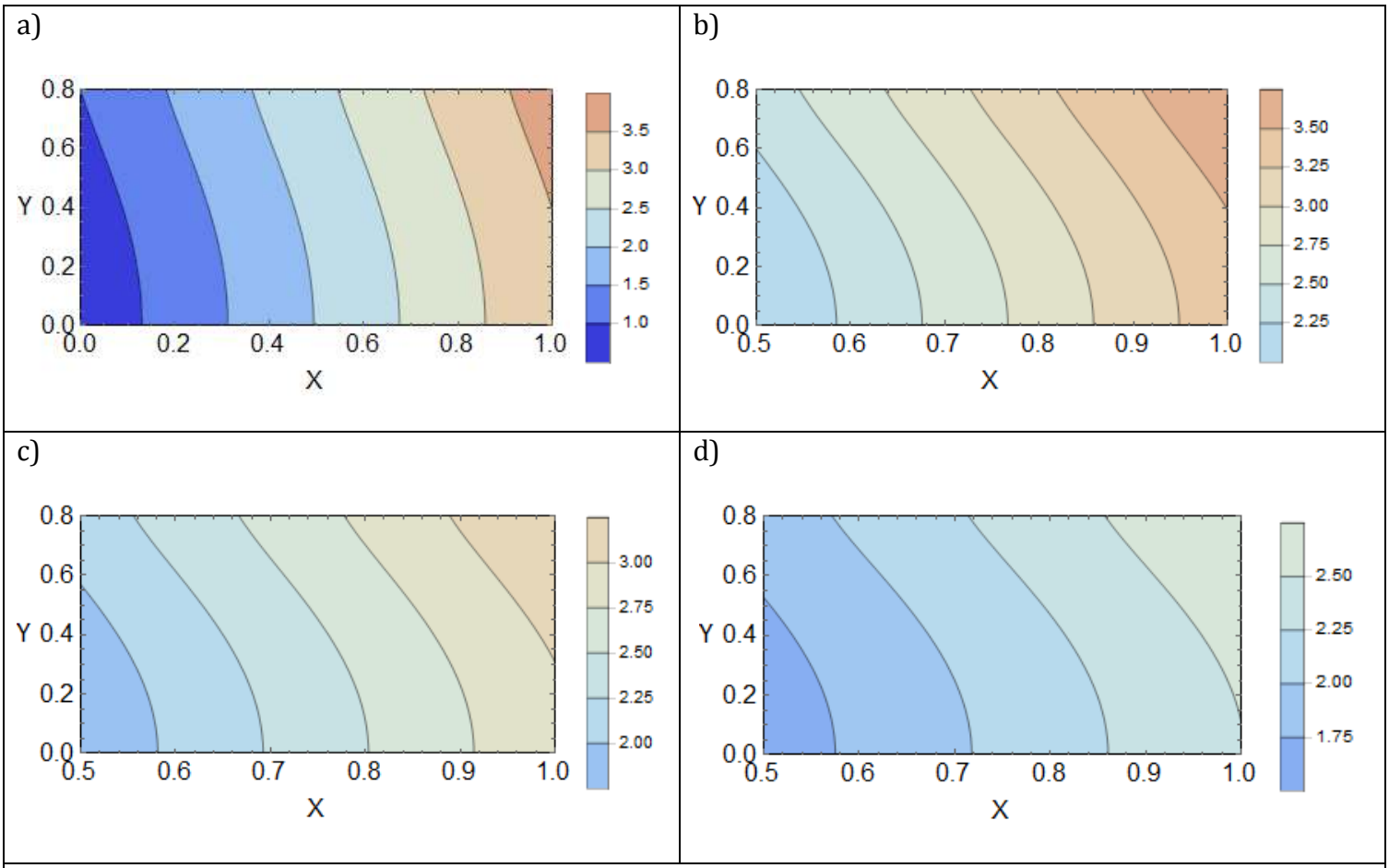

Fig. 6. Dimensionless concentration contours for varying Damköhler number,γ, a) showing the full microchannel for $= 1.1$, b) mid-section of microchannel for $\gamma = 1.1$, c) mid-section for $\gamma = 0.9$, and d) mid-section for $\gamma = 0.7$.

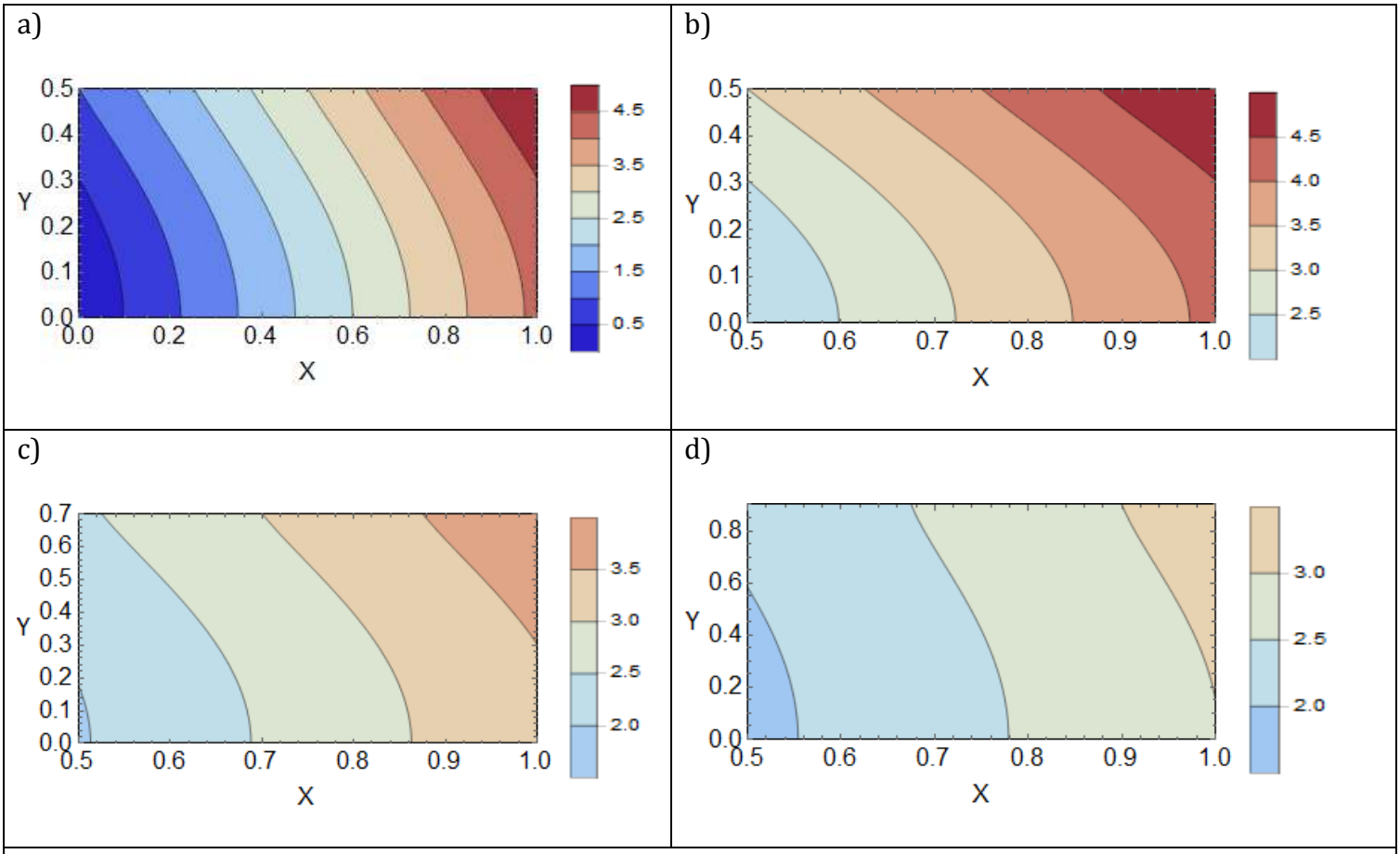

Fig. 7. Dimensionless concentration contours for varying wall thickness, Y_1, a) showing the full microchannel for $Y_1 = 0.5$, b) mi-section of microchannel, for $Y_1 = 0.5$, c) mid-section for $Y_1 = 0.7$, and d) mid-section for $Y_1 = 0.9$.

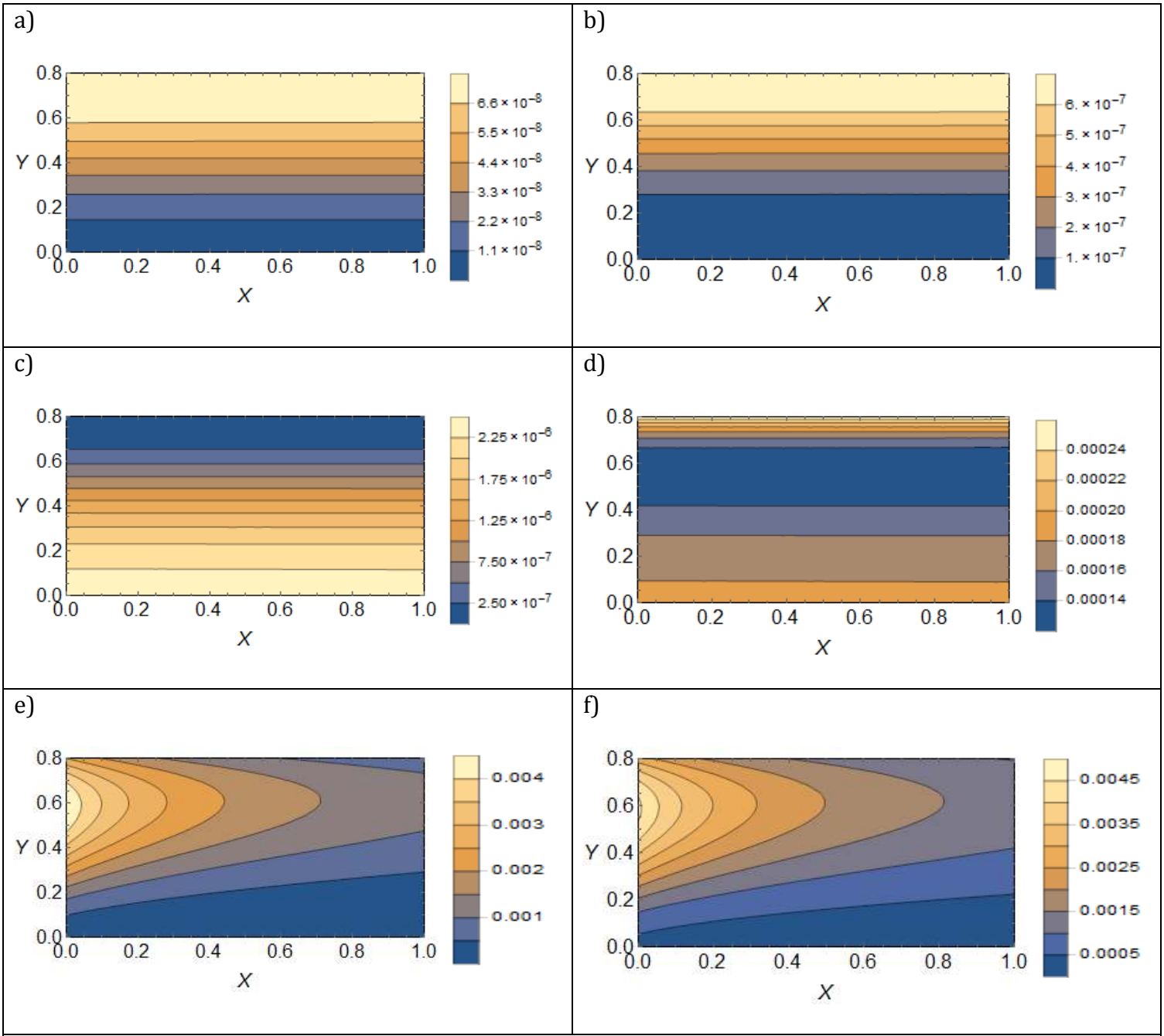

Fig 8. Local entropy generation contours for the base configuration showing a)$N_{s,ht}$, b) $N_{f,ht}$, c)N_{int}, d)N_{FF}, e)N_{DI} and f)N_{pm}.

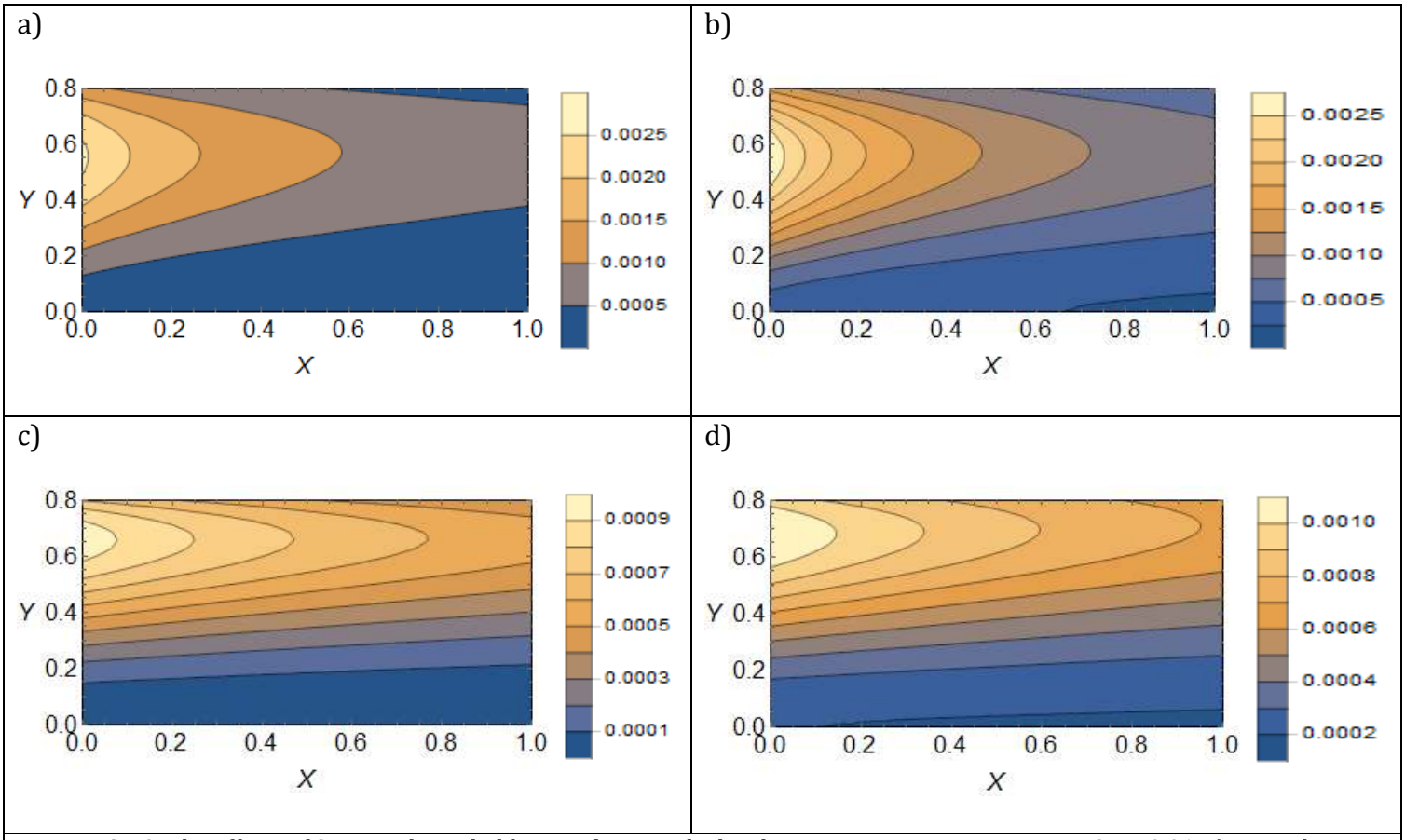

Fig. 9. The effects of Soret and Damköhler numbers on the local entropy generation, top row: $Sr = 0.01$, a)N_{DI} and b)N_{pm}, bottom row: $\gamma = 0.3$, c)N_{DI} and d)N_{pm}.

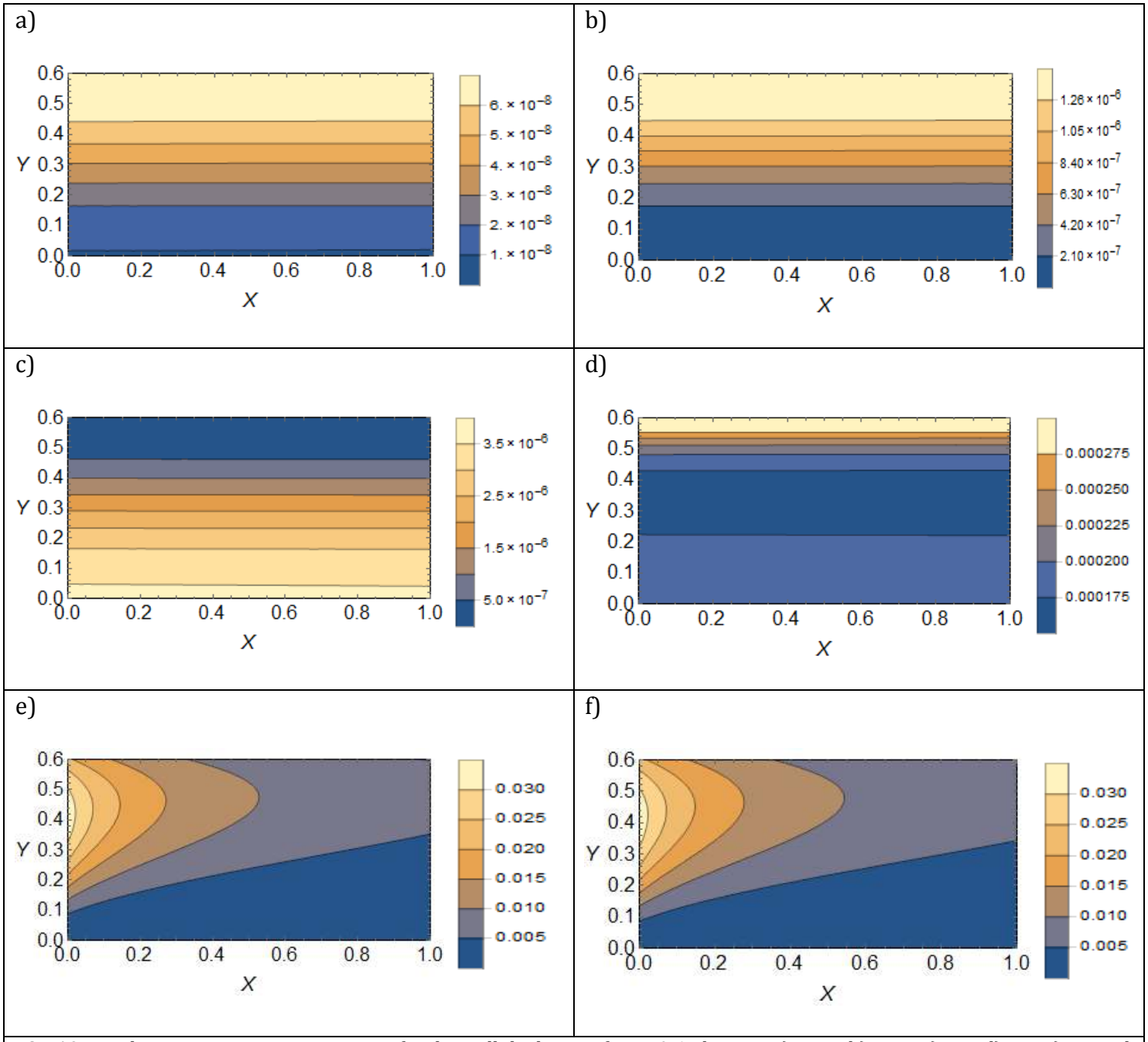

Fig. 10. Local entropy generation contours for the wall thickness of $Y_1 = 0.6$, showing a)$N_{s,ht}$, b) $N_{f,ht}$, c)N_{int}, d)N_{FF}, e)N_{DI} and f)N_{pm}.

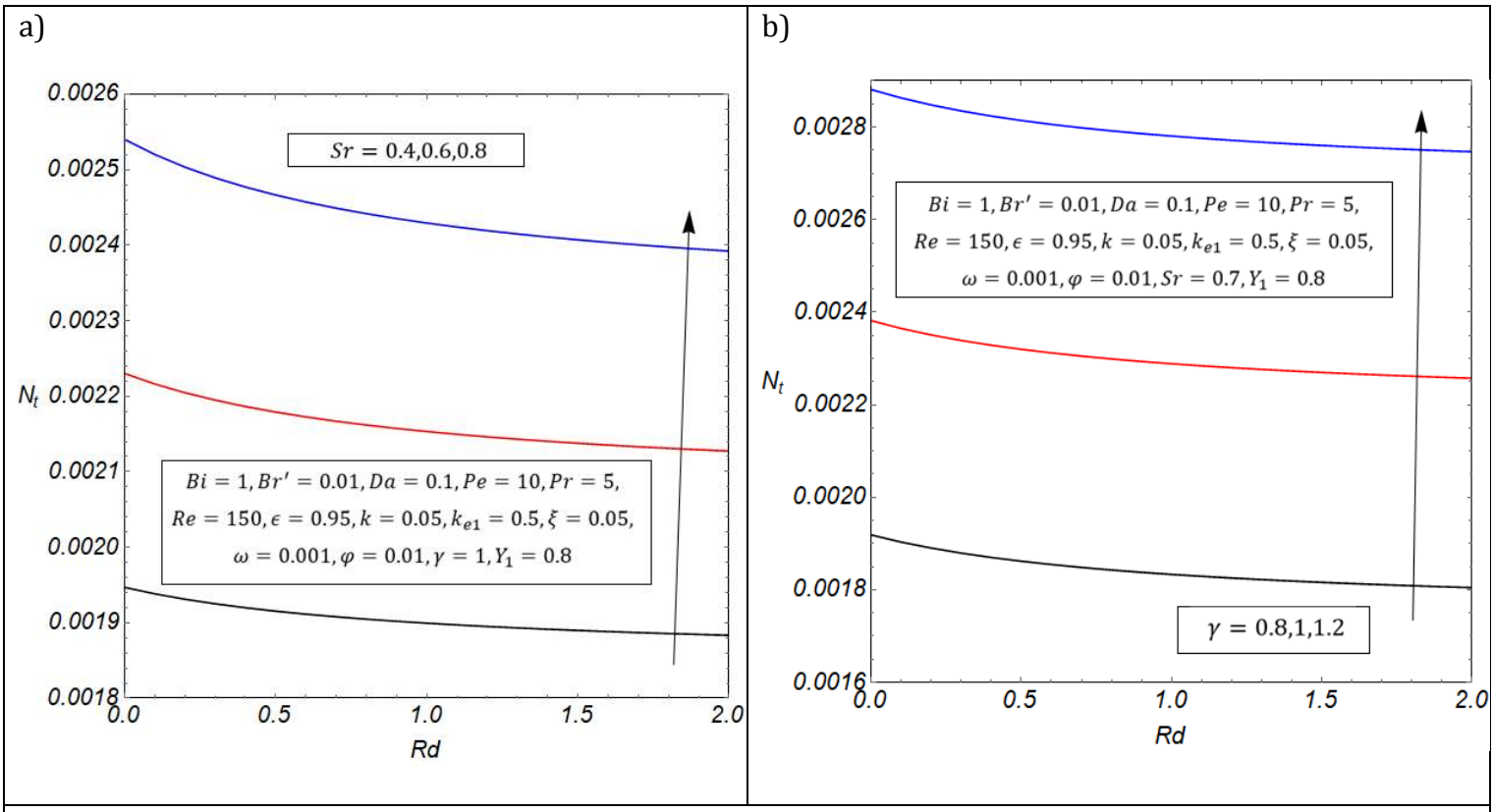

Fig. 11. Total Entropy generation graphs for varying radiation parameter, Rd, with various values of a) Soret number, Sr and b) Damköhler number, γ.

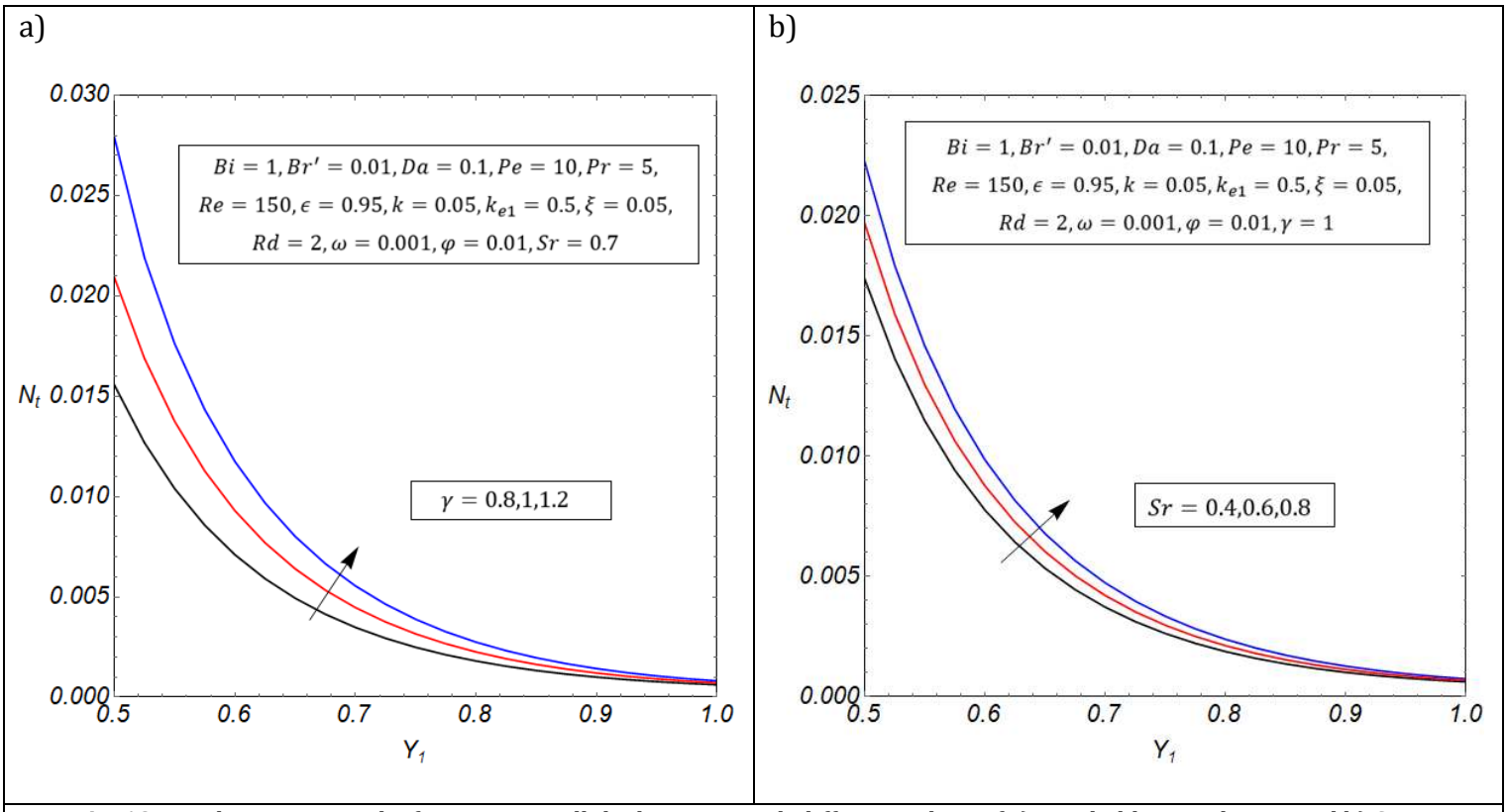

Fig. 12. Total Entropy graphs for varying wall thickness, Y_1 with different values of a) Damköhler number, γ, and b) Soret number, Sr.

Table 1. List of base parameters values used in the production of all graphs except where otherwise stated.	
Symbol	**Value**
Bi	1
Br'	0.01
γ	1
Da	0.1
Pe	10
Pr	5
Re	150
Sr	0.7
ϵ	0.95
k	0.05
k_{e1}	0.5
ω	0.001
φ	0.01
Y_1	0.8
ξ	0.05
Rd	2